

International Journal of Multiphase Flow

Comparative Study of Flow-Rate Dependence and End Effects in Steady-State Two-Phase Flow through Model Pore Networks

--Manuscript Draft--

Manuscript Number:	
Article Type:	Research paper
Keywords:	porous media; Two-phase Flow; relative permeability; wettability; intrinsic dynamic capillary pressure; SCAL
Corresponding Author:	Marios Valavanides, Ph.D. University of West Attica GREECE
First Author:	Marios Valavanides
Order of Authors:	Marios Valavanides Konstantinos Mouravas, PhD student Nikolaos Karadimitriou, Ph.D. Panayiotis Dimitriadis, Ph.D. Andreas Yiotis, Assitant Professor Holger Steeb, Professor
Abstract:	<p>This study investigates the influence of network geometry, wettability, and flow conditions on end effects during steady-state immiscible two-phase flow in model pore networks. Systematic co-injection experiments were performed in planar microfluidic networks with periodic and non-periodic geometries and varying wettability characteristics, enabling direct comparison over a broad range of flow conditions, expressed in terms of capillary number and flow-rate ratio. Using the DeProF theoretical framework, pressure-drop measurements were analyzed to evaluate the flow-rate-dependency of relative permeabilities, intrinsic dynamic capillary pressure, and energy efficiency. In parallel, sub-pore-scale imaging provided direct insight into the spatiotemporal evolution of interstitial flow structures under both steady and transient flow conditions. The study: (a) further validates the DeProF framework as a robust and efficient approach for analyzing two-phase flow in porous media, capturing flow-rate dependency and energy efficiency across diverse flow conditions, fluid pairs, and pore-network configurations; and (b) demonstrates its potential to infer interstitial flow-structure characteristics from ex-core (macroscopic) relative permeability measurements. The results show that system-specific correlations can be established between macroscopic flow measurements at critical flow conditions and the underlying interstitial flow structures. These findings support the development of flow-dependent relative permeability scaling models and improved special core analysis (SCAL) protocols that more accurately capture the physics governing two-phase flow in natural porous media.</p>
Opposed Reviewers:	

International Journal of Multiphase Flow, Elsevier

Dear Editor,

Please find attached our manuscript entitled

“Comparative Study of Flow-Rate Dependence and End Effects in Steady-State Two-Phase Flow through Model Pore Networks”

by

Mouravas, K., Karadimitriou, N., Dimitriadis, P., Yiotis, A., Steeb, H., and Valavanides, M.,

submitted for consideration for publication in the ***International Journal of Multiphase Flow***.

The manuscript presents an experimental and theoretical investigation of steady-state immiscible two-phase flow in model pore networks, with emphasis on flow-rate dependence, end effects, and the relationship between macroscopic flow properties and pore-scale flow structures.

We believe the work is well aligned with the scope of the journal and will be of interest to researchers working in porous-media flow, multiphase transport, and geoenery applications.

Thank you for your consideration. We look forward to your response.

Sincerely,

Marios Valavanides

Comparative Study of Flow-Rate Dependence and End Effects in Steady-State Two-Phase Flow through Model Pore Networks

Mouravas, K.^{1,2}, Karadimitriou, N.², Dimitriadis, P.¹, Yiotis, A.³, Steeb, H.^{2,4} and Valavanides, M.^{1*}

¹Dept of Civil Engineering, University of West Attica, 12241 Egaleo Attica, Greece

²Institute of Applied Mechanics, University of Stuttgart, 70569 Stuttgart, Germany

³School of Rural, Surveying & GIS Eng., National Technical Univ. of Athens, Greece

⁴Stuttgart Center for Simulation Science (SC SimTech), 70569 Stuttgart, Germany

* Corresponding author marval@uniwa.gr

Highlights

- *Influence of pore-network geometry, wettability, and flow conditions on end effects was systematically investigated.*
- *Steady-state two-phase flow experiments were conducted in planar microfluidic pore networks.*
- *DeProF analysis quantified flow-rate-dependent relative permeability, dynamic capillary pressure, and energy efficiency.*
- *Sub-pore-scale imaging revealed the evolution of interstitial flow structures under transient and steady conditions.*
- *Macroscopic flow measurements were correlated with underlying pore-scale flow structures.*
- *Results support improved flow-dependent SCAL protocols and relative permeability scaling models.*

Comparative Study of Flow-Rate Dependence and End Effects in Steady-State Two-Phase Flow through Model Pore Networks

Mouravas, K.^{1,2}, Karadimitriou, N.², Dimitriadis, P.¹, Yiotis, A.³, Steeb, H.^{2,4} and Valavanides, M.^{1*}

¹Dept of Civil Engineering, University of West Attica, 12241 Egaleo Attica, Greece

²Institute of Applied Mechanics, University of Stuttgart, 70569 Stuttgart, Germany

³School of Rural, Surveying & GIS Eng., National Technical Univ. of Athens, Greece

⁴Stuttgart Center for Simulation Science (SC SimTech), 70569 Stuttgart, Germany

* Corresponding author marval@uniwa.gr

Keywords: *porous media, two-phase flow, relative permeability, flow-rate dependency, intrinsic dynamic capillary pressure, SCAL, microfluidics.*

Abstract.

This study investigates the influence of network geometry, wettability, and flow conditions on end effects during steady-state immiscible two-phase flow in model pore networks. Systematic co-injection experiments were performed in planar microfluidic networks with periodic and non-periodic geometries and varying wettability characteristics, enabling direct comparison over a broad range of flow conditions, expressed in terms of capillary number and flow-rate ratio.

Using the DeProF theoretical framework, pressure-drop measurements were analyzed to evaluate the flow-rate-dependency of relative permeabilities, intrinsic dynamic capillary pressure, and energy efficiency. In parallel, sub-pore-scale imaging provided direct insight into the spatiotemporal evolution of interstitial flow structures under both steady and transient flow conditions.

The study: (a) further validates the DeProF framework as a robust and efficient approach for analyzing two-phase flow in porous media, capturing flow-rate dependency and energy efficiency across diverse flow conditions, fluid pairs, and pore-network configurations; and (b) demonstrates its potential to infer interstitial flow-structure characteristics from ex-core (macroscopic) relative permeability measurements.

The results show that system-specific correlations can be established between macroscopic flow measurements at critical flow conditions and the underlying interstitial flow structures. These findings support the development of flow-dependent relative permeability scaling models and improved special core analysis (SCAL) protocols that more accurately capture the physics governing two-phase flow in natural porous media.

36

NOMENCLATURE

37

Subscripts, superscripts etc.

38 ~

A tilde above a letter indicates a dimensional variable; no tilde above a letter denotes a dimensionless variable

39

40 ;

A semicolon separates the group of a function's arguments into independent variables and system parameters.

41

42 *

An asterisk (as superscript) indicates a value corresponding to critical flow conditions

43

44 n

index (subscript) indicating a non-wetting phase variable

45 w

index (subscript) indicating a wetting phase variable

46 i, j, k, m indices

47

Physical variables – Latin letters

48 Ca

Capillary number

49 f_{EU}

energy utilization factor, or, energy efficiency

50 f

fractional flow

51 \tilde{k}

absolute permeability of the porous medium

52 k_r

relative permeability

53 \tilde{p}

macroscopic pressure

54 r

non-wetting phase /wetting-phase flow-rate ratio

55 S_w

wetting phase saturation

56 \tilde{q}

flow-rate

57 U

superficial velocity, or, flow intensity

58 x

reduced macroscopic pressure gradient

59 \tilde{z}

coordinate length along the macroscopic flow direction

60

Physical variables - Greek letters

61 $\tilde{\gamma}_{nw}$

interfacial tension between the wetting and the non-wetting phase

62 θ_A

dynamic contact angle for advancing meniscus

63 θ_R

dynamic contact angle for receding meniscus

64 κ

non-wetting/wetting phase viscosity ratio

65 λ

non-wetting/wetting phase mobility ratio

66 $\tilde{\mu}$

dynamic viscosity

67

Abbreviations

68	CFC(s)	critical flow condition(s)
69	IDCP	Intrinsic Dynamic Capillary Pressure
70	n/w	non-wetting phase /wetting phase
71	REV	Representative Elementary Volume
72	SCAL	Special Core Analysis Laboratory

73 **1 Introduction**

74 Two-phase flow in porous media is a fundamental process underpinning a wide range of
 75 energy and environmental applications, including enhanced oil recovery, CO₂ sequestration,
 76 geothermal energy storage, groundwater remediation, operation of trickle bed reactors and
 77 fuel cells, etc. The flow system comprises two immiscible phases flowing simultaneously
 78 through a complex network of interconnected pores. In such systems, one of the two phases,
 79 the *wetting phase*, WP, preferentially wets the solid surface against the other, *non-wetting*
 80 *phase*, NWP. The degree of wettability is governed by the physicochemical affinities between
 81 the two fluids and the solid matrix.

82 In general, the aforementioned processes span a wide range of spatial and temporal scales:
 83 pore-scale phenomena occur at micrometer to millimeter scales, while field-scale behavior
 84 extends from meters to a few hundreds of meters, **Figure 1**. Correspondingly, the governing
 85 mechanisms must be described within a hierarchical, multiscale framework. At the pore /
 86 microscopic scale, highly nonlinear interactions dominate a variety of intrinsic flow
 87 phenomena, whereas at the macroscopic scales flow is typically described within a
 88 *representative elementary volume* (REV), where the flow system is treated as an effective
 89 mixture of interacting continua. The flow dynamics are primarily controlled by momentum
 90 transport associated with two competing mechanisms: capillary forces, arising from
 91 interfacial curvature (Young–Laplace / wettability effects), and viscous forces, described by
 92 Navier–Stokes flow within the pore network.

93 The transition from pore-scale to REV-scale relies on spatial averaging (upscaling),
 94 whereby the ensemble of interfacial and viscous interactions are integrated into
 95 phenomenological constitutive relations. These relations, such as fractional-flow extensions
 96 of Darcy’s law, link average phase fluxes to pressure gradients and form the basis for
 97 continuum-scale modeling and simulation [Dullien, 1992; Bear, 2018]. Importantly, the
 98 definition of an REV is scale-dependent and problem-specific, particularly in multiscale or
 99 multiphysics systems where different flow components may exhibit distinct characteristic
 100 sizes and volumetric fractions.

101 Albeit two-phase flow in porous media is central to a wide spectrum of energy and
 102 environmental technologies, its macroscopic description remains fundamentally incomplete.
 103 In practice, the phenomenology of steady-state two-phase flow in porous media is recorded in

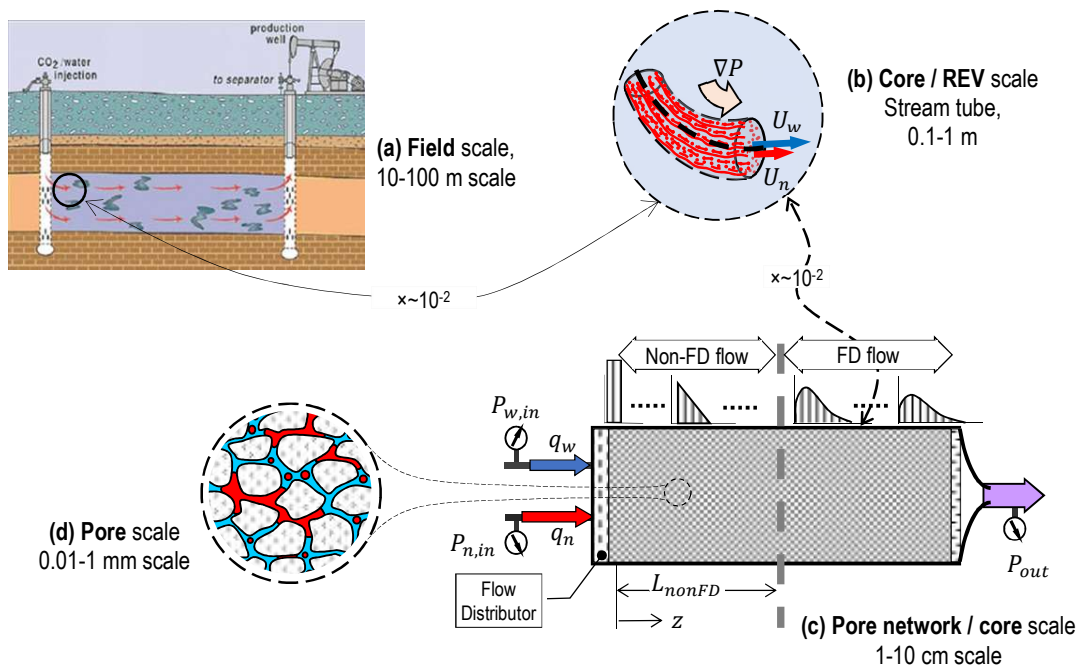
104 diagrams of relative permeabilities obtained through systematic experimental studies in
105 *Special Core Analysis Laboratory* (SCAL) interventions. In these experiments, proxy fluid
106 phases are co-injected through core samples under controlled flow conditions and pressure
107 drops are measured to infer relative permeabilities via generalized (i.e. multiphase) Darcy-
108 type relations, **Figure 1(c)**. Advanced imaging techniques, including X-ray micro-computed
109 tomography (μ XRCT) [Georgiadis *et al.*, 2013; Wildenschild & Sheppard, 2013; Oughanem
110 *et al.*, 2015; Youssef *et al.*, 2017; Andrew *et al.*, 2015; Pak *et al.*, 2015] have further
111 enhanced insight into pore-scale flow structures, enabling direct observation of saturation
112 distributions and dynamic events such as Haines jumps [Berg *et al.*, 2013] or contact angle
113 variations [Singh *et al.*, 2016]. Downstream the application pathway, the resulting core-scale
114 REV descriptions are implemented in reservoir simulators for field-scale predictions.

115 The conventional framework based on fractional extensions of Darcy's law, rooted in
116 saturation-dependent relative permeability functions, is also applied in SCAL measurements
117 that traditionally express relative permeability as a function of phase saturation. However,
118 theoretical inferences [Valavanides & Payatakes, 2001; Valavanides, 2018(b)], supported by
119 numerical [Constantinides & Payatakes, 1989; 2000; Valavanides *et al.*, 1998; Blunt *et al.*,
120 2002; Nguyen *et al.*, 2006; Sinha *et al.*, 2017; 2021; Valavanides, 2018(a); Yiotis *et al.*,
121 2019], and experimental evidence [Wyckoff & Botset, 1936; Avraam & Payatakes, 1995;
122 1999; Wildenschild *et al.*, 2001; Tallakstad *et al.*, 2009; Datta *et al.*, 2014; Youssef *et al.*,
123 2014; Rücker *et al.*, 2015; Tsakiroglou *et al.*, 2015; Armstrong *et al.*, 2016; Zou *et al.*, 2018;
124 Gao *et al.*, 2020; Valavanides *et al.*, 2020; Zhang *et al.*, 2021; Karadimitriou *et al.*, 2023],
125 indicates that steady-state flow behavior depends not only on saturation, but also explicitly on
126 flow conditions, particularly in regimes where capillary and viscous forces are comparable,
127 and disconnected non-wetting phase structures (ganglia and droplets) remain mobile through
128 dynamic connectivity in intermittent micro-flows [Reynolds *et al.*, 2017; Spurin *et al.*, 2019;
129 Anastasiou *et al.*, 2024; Wang *et al.*, 2025]. The take away message is that widely used
130 relative permeability models based on saturation dependency lack universality and often fail
131 to provide predictive accuracy outside the narrow conditions under which they are calibrated.
132 These findings motivate the development of flow-dependent constitutive models,
133 implementing different upscaling approaches, based on pure mechanistic or hybrid
134 mechanistic-thermodynamic-stochastic analyses [Berg *et al.*, 2026].

135 SCAL experiments form the cornerstone of industrial practice for characterizing two-
136 phase flow in natural porous media [API, 1998; McPhee, 2015]. Yet, a critical challenge in
137 SCAL is the presence of so-called *end effects*, arising from the abrupt transition from single-
138 phase flow in inlet tubing into two-phase flow within the porous medium. This transition
139 induces a spatial reorganization of the flow structure past the inlet, before a fully developed
140 (FD) state is reached further downstream, **Figure 1(c)**. Consequently, a non-negligible
141 portion of the core operates under transient or evolving flow conditions (non-fully developed,
142 non-FD), even when macroscopic steady state appears to have been established. This directly
143 violates the underlying premise of REV-scale modeling and introduces a latent bias in

144 measured pressure gradients and inferred relative permeabilities. Despite the efforts to
 145 correctly reproduce the real flow conditions (steady-state or transient, drainage or imbibition,
 146 confining /overburden pressure and temperature) as well as system properties (viscosity ratio,
 147 wettability and other physicochemical properties of the proxy fluids), end effects pose an
 148 inherently critical problem in SCAL. They bias the interpretation of any relation between the
 149 measured values of the physical quantities (pressure gradients, saturation and flow-rates),
 150 thereby compromising the validity of the inferred REV-scale constitutive relations. End
 151 effects may be substantial or not, depending on the extent of the non-FD zone relative to the
 152 core length. Their magnitude depends on flow conditions, fluid properties, as well as pore
 153 network characteristics and overall length, and they are particularly pronounced in low
 154 capillary number regimes.

155



156

157 **Figure 1** Typical up-scaling / down-scaling implemented in modeling two-phase flow
 158 in porous media. (a) The field scale. (b) The Darcy (or REV stream tube) scale of the
 159 fractional flow, constitutive model. (c) The core, or network scale model, and imposed flow
 160 conditions; the evolution of the flow structure is exhibited by representative size distributions
 161 of the disconnected non wetting phase elements. (d) The pore-scale model whereby the
 162 virtual magnification depicts the internal structure of the composite flow within the core of a
 163 porous medium at the scale of a few pores; the disconnected non wetting phase (in red) is
 164 dispersed within the continuous wetting phase (in light blue).

165

166 In that context, end effects distort the trueness of the REV constitutive relations and,
 167 consequently, the specificity of field-scale simulators. End effects are typically treated as
 168 experimental artefacts –to be minimized– rather than as intrinsic features of the flow that
 169 must be quantified and incorporated into modeling frameworks. Crucially, there is currently
 170 no systematic methodology to assess their impact using standard SCAL measurements, nor a

171 clear understanding of how they depend on flow regime, wettability, and pore network
172 geometry.

173 The present study addresses this gap by pursuing two objectives: (i) to examine if end
174 effects contribute systematically –and predictably– to the observed flow structure,
175 particularly in low capillary number and low flow rate ratio regimes, and (ii) to investigate
176 whether their signature can be extracted from conventional, ex-core measurements alone,
177 bypassing any direct access to interstitial, pore-scale information.

178 To achieve this, we extend a precursor study in microfluidic network [Karadimitriou *et al.*,
179 2023] by decoupling the roles of pore geometry and wettability. To this end we deploy
180 systematic experiments in both periodic and non-periodic microfluidic, planar model pore
181 networks fabricated from different materials. In parallel, we take advantage of the
182 transparency of the matrix material and introduce an imaging-based methodology to resolve
183 the spatiotemporal evolution of flow structures, enabling direct correlation between
184 interstitial flow structure and external measurements. This approach allows us to identify
185 characteristic invariants of the flow and to reinterpret SCAL data within a flow-structure-
186 informed framework consistent with the hybrid mechanistic-stochastic theoretical framework
187 of *Decomposition in Prototype Flows (DeProF)* [Valavanides, 2018(b); 2023] (the DeProF
188 paradigm).

189 Our study provides evidence that end effects are integral components of the observed flow
190 response, with measurable impact on REV-scale constitutive relations. This challenges the
191 conventional interpretation of SCAL measurements in terms of saturation dependency and
192 calls for a revision of standard protocols, accounting for flow rate dependency of relative
193 permeabilities. In parallel, it establishes a pathway to infer flow-structure information from
194 macroscopic observables, and contributes toward the development of flow-dependent, true-
195 to-mechanism relative permeability models with improved specificity.

196 The paper is organized in 4 sections, including this introductory section. Section 2
197 provides the theoretical framework, i.e. a basic analysis of steady-state, two-phase flow in
198 porous media, and a discussion on the concept of fully-developed flow conditions and end
199 effects when porous media specimens of finite length are examined. Section 3 describes the
200 materials and laboratory workflow of the experiments. Section 4 presents the results of study
201 and discusses the potential for improving SCAL protocols.

202 **2 Basic theoretical framework**

203 For the self-sufficiency of the current work, we present here the basic theoretical framework,
204 developed by Valavanides [2018; 2023] for the energy and flowrate-dependency analysis of
205 steady-state two-phase flow in pore networks.

206 *2.1 Basic considerations*

207 Consider the simultaneous, one-dimensional concurrent flow of a non-wetting phase (NWP),

208 and a wetting phase (WP), both incompressible through a porous medium (PM). The
 209 variables pertaining to the NWP are indexed with n , whereas those pertaining to the WP are
 210 indexed with w . Note, a tilde (\sim) embellishment indicates a dimensional variable, otherwise
 211 the variable is dimensionless.

212 The two phases flow across a porous medium control surface with cross-sectional area, \tilde{A} ,
 213 with flow rates \tilde{q}_n and \tilde{q}_w , respectively. Average corresponding pressure gradients,
 214 $(\Delta\tilde{p}/\Delta\tilde{z})_w$ and $(\Delta\tilde{p}/\Delta\tilde{z})_n$ are induced upon the two phases. The term ‘‘average’’ refers to the
 215 representative elementary volume (REV) average. This type of two-phase flow is described
 216 by the set of phenomenological, fractional flow, Darcy-type relations,

$$\frac{\tilde{q}_n}{\tilde{A}} \equiv \tilde{U}_n = \frac{\tilde{k}}{\tilde{\mu}_n} k_{rn} \left(\frac{\Delta\tilde{p}}{\Delta\tilde{z}} \right)_n \quad \text{and} \quad \frac{\tilde{q}_w}{\tilde{A}} \equiv \tilde{U}_w = \frac{\tilde{k}}{\tilde{\mu}_w} k_{rw} \left(\frac{\Delta\tilde{p}}{\Delta\tilde{z}} \right)_w \quad (1)$$

217 where,

218 \tilde{U}_w, \tilde{U}_n are the superficial velocities, $\tilde{\mu}_w, \tilde{\mu}_n$ are the dynamic phase viscosities, and \tilde{k} is the
 219 absolute (intrinsic) permeability of the pore network.

220 The flow rate ratio of the two phases, r , is defined as,

$$r = \tilde{q}_n / \tilde{q}_w = \tilde{U}_n / \tilde{U}_w \quad (2)$$

221 and is essentially a *kinematic* property of the flow.

222 The mobility ratio, λ , is defined as the ratio of the mobilities,

$$\lambda = \frac{\tilde{\lambda}_n}{\tilde{\lambda}_w} = \frac{(k_{rn}/\tilde{\mu}_n)(\Delta\tilde{p}/\Delta\tilde{z})_n}{(k_{rw}/\tilde{\mu}_w)(\Delta\tilde{p}/\Delta\tilde{z})_w} = \frac{1}{\kappa} \frac{k_{rn}}{k_{rw}} \frac{(\Delta\tilde{p}/\Delta\tilde{z})_n}{(\Delta\tilde{p}/\Delta\tilde{z})_w} \quad (3)$$

223 and is essentially a *kinetic* property of the flow as it relays to the pressure gradients,
 224 $(\Delta\tilde{p}/\Delta\tilde{z})_i$, $i = n, w$.

225 where the NWP/WP bulk viscosity ratio, κ , is defined as

$$\kappa = \tilde{\mu}_n / \tilde{\mu}_w \quad (4)$$

226 The average intrinsic capillary pressure is

$$\tilde{p}_c(\tilde{z}) \equiv \tilde{p}_n(\tilde{z}) - \tilde{p}_w(\tilde{z}) \quad (5)$$

227 where $\tilde{p}_n(\tilde{z})$, $\tilde{p}_w(\tilde{z})$, are the average bulk pressures in the NWP and WP respectively (see
 228 also [Valavanides, 2023, Appendix I]. This definition is in line with the definition provided
 229 by Bear [2018, Eq. 6.1.1]. Note that Eq. (5) provides a measure of the capillary pressure jump
 230 across the two bulk phase pressures due to the combined effect of Young-Laplace capillary
 231 forces acting across all NWP/WP menisci. So long as the NWP is disconnected, to a larger or
 232 smaller extent, $\tilde{p}_c(\tilde{z}) > 0$.

233 2.2 *Non-fully and fully developed flow*

234 When the fluids are co-injected at constant (but generally different) flow-rates, they gradually
 235 evolve from uncoupled, single phase Poiseuille-type flow within the injecting tubes, to a
 236 complex two-phase network-flow system. Downstream the inlet ports, the NWP disconnects
 237 into fluidic elements, i.e. ganglia of relatively large or small size and/or droplets (see e.g.
 238 Anastasiou *et al.*, 2024), that interact with each other and the WP by exchanging momentum
 239 across their interfaces. The interstitial structure of this flow system can be described by an
 240 evolving size distribution of disconnected NWP fluidic elements (ganglia, droplets), **Figure**
 241 **1(c)** [Valavanides *et al.*, 1998]. The interstitial flow structure at any position downstream the
 242 entry ports can be described – at increasing levels of resolution – by saturation, fractional
 243 flows of droplets, ganglia and connected pathways (i.e. super-long or percolating ganglia)
 244 and ganglion size distributions [Valavanides, 2018(a)]. The local flow at any cross-section
 245 takes a steady-state, time-average configuration, described by an ensemble of incessant,
 246 instantaneous *physically admissible flow configurations* or *flow microstates* [Valavanides &
 247 Daras, 2016, Valavanides, 2018(a)]. As it evolves downstream the inlet ports, it is *non-fully*
 248 *developed*. If the network, or the core, is adequately long and relatively homogeneous, then,
 249 far downstream the inlet ports, the flow system will eventually reach a *fully developed* state,
 250 where the partitioning of NWP among the above-mentioned configurations remains
 251 practically constant with both time and along the main flow direction. Attaining a fully
 252 developed state is not always possible. That depends on the combination of the flow
 253 conditions, the physicochemical properties of the fluids and the structure of the pore network.
 254 Most critical is the role of the relative magnitude of the viscous forces over capillary forces,
 255 and the heterogeneity properties of the network. Exhibits of transitions of interstitial flow
 256 from non-fully developed to fully-developed structures can be found in [Aursjo *et al.*, 2014].

257 When the flow system has reached a fully developed (FD) state, the local capillary
 258 pressure remains constant and the two local pressure gradients pertaining to the NWP and the
 259 WP, become equal,

$$\text{fully developed flow: } \left(\frac{\Delta\tilde{p}}{\Delta\tilde{z}} \right) \approx \left(\frac{\Delta\tilde{p}}{\Delta\tilde{z}} \right)_w \approx \left(\frac{\Delta\tilde{p}}{\Delta\tilde{z}} \right)_n \quad (6)$$

260 Therefore, the phenomenological, Darcy type, fractional flow relations that describe the
 261 steady-state fully developed flow become,

$$\frac{\tilde{q}_n}{\tilde{A}} \equiv \tilde{U}_n = \frac{\tilde{k}}{\tilde{\mu}_n} k_{rn} \left(\frac{\Delta\tilde{p}}{\Delta\tilde{z}} \right) \quad \text{and} \quad \frac{\tilde{q}_w}{\tilde{A}} \equiv \tilde{U}_w = \frac{\tilde{k}}{\tilde{\mu}_w} k_{rw} \left(\frac{\Delta\tilde{p}}{\Delta\tilde{z}} \right) \quad (7)$$

262 and, under such conditions, the common pressure gradient in both phases can be expressed in
 263 reduced form,

$$x = \frac{\Delta\tilde{p}/\Delta\tilde{z}}{(\Delta\tilde{p}/\Delta\tilde{z})^{1\Phi}} = \frac{\Delta\tilde{p}}{\Delta\tilde{z}} \frac{\tilde{k}}{\tilde{\mu}_w \tilde{U}_w} = \frac{\Delta\tilde{p}/\Delta\tilde{z}}{\tilde{\gamma}_{nw} C a / k} = \frac{\Delta\tilde{p}}{\Delta\tilde{z}} \frac{\tilde{k}}{\tilde{\mu}_w \tilde{U}_w} = \frac{1}{k_{rw}} \quad (8)$$

264 where

265 $(\Delta\tilde{p}/\Delta\tilde{z})^{1\Phi}$ is the pressure gradient corresponding to an equivalent saturated single-phase
 266 flow (1Φ) of the WP at the same superficial velocity \tilde{U}_w
 267 Ca is the capillary number, conventionally expressed as

$$Ca = \frac{\tilde{\mu}_w \tilde{U}_w}{\tilde{\gamma}_{nw}} \quad (9)$$

268 where $\tilde{\gamma}_{nw}$ is the interfacial tension between the two phases. This particular expression is only
 269 nominal; it fails to capture the true physics behind the definition of the capillary number, as
 270 the ratio of the viscous to the capillary forces, especially when both phases are mobile. Please
 271 note that this expression is strict /correct only when the saturation of the NWP is approaching
 272 zero and the sparse disconnected NWP elements are immobile. In case of two-phase flow, the
 273 expression in eqn (9) fails to account for the viscous forces, from the bulk flow of both
 274 phases, as well as the effective capillary forces due to the motion of the n/w menisci through
 275 the tortuous network. The issue has been discussed in [Valavanides, 2018(b)] where he
 276 introduced the concept of an effective capillary number, and recently by [Yang *et al.*, 2026].

277 Note that, by definition, the reduced pressure gradient is essentially the inverse of the
 278 relative permeability of the WP [see far right side of eqn (8)]. Moreover, the set of
 279 superficial velocities in eqs (7) may be appropriately reduced and replaced by a set of
 280 dimensionless variables, namely, the capillary number, Ca , eqn (9), and the NWP/WP flow-
 281 rate ratio, r , eqn (2).

282 At steady-state conditions, if and only if the flow is fully developed (FD), i.e. there are
 283 either no capillary end effects or these can be considered to be negligible, the flow-rate ratio,
 284 r , becomes equal to the mobility ratio, λ .

$$FD \text{ flow: } r = \frac{U_n}{U_w} \equiv \frac{1}{\kappa} \frac{k_{rn}}{k_{rw}} = \lambda \quad \Leftrightarrow \quad k_{rn} = \kappa r k_{rw} \quad (10)$$

285 In fully developed flows, because of the common pressure gradient, eqs (7) or (8) and the
 286 equivalence between flow-rate ratio and mobility ratio, eqn (10)), relative permeability
 287 curves intersect at a fixed value of the flow-rate ratio, the so-called relative permeability
 288 cross-over value, r_x . The latter is equal to the inverse of the viscosity ratio [Valavanides,
 289 2023],

$$r_x = 1/\kappa \quad (11)$$

290 This inherent characteristic of steady-state, fully developed flows, eqs. (10) and (11), may
 291 be used in assessing the presence of capillary end effects when reviewing relative
 292 permeability data collected during SCAL. If the imposed flow-rate ratio values, r_i , and the
 293 corresponding measured mobility ratio values, λ_i , are equal, then fully developed flow
 294 conditions have settled-in and end effects are considered to be negligible. Ideally, in absence
 295 of end effects, then, all pairs of $\{r_i, \lambda_i\}$ align on a straight line with inclination 1:1. In
 296 practice, when SCAL measurements are examined, the equality expressed by eqn (10), could

297 be used as a soft criterion in verifying the absence or negligibility of end effects. We have
 298 applied this criterion in the current study.

299 2.3 Energy efficiency & independent variables

300 The energy efficiency of the process is defined [Valavanides, 2018(b)] as the flow-rate of the
 301 NWP per unit of total hydraulic power spent, or equivalently, provided externally to the
 302 NWP/WP/PM system by the injection pumps, to maintain two-phase flow at any set of
 303 externally imposed flow conditions, i.e., Ca and r . The associated *energy efficiency index*,
 304 f_{EU} , can be readily calculated in terms of macroscopic measurements, as

$$f_{EU} = \frac{k_{rn}}{\kappa(r+1)} = \frac{rk_{rw}}{r+1} = \frac{r}{x(r+1)} \quad (12)$$

305 An important characteristic of two-phase flow in porous media is that for every fixed
 306 value of the capillary number, Ca , there exists a single value of the flow-rate ratio, r^* , for
 307 which the energy efficiency index, f_{EU}^* , attains a maximum value [Valavanides et al., 2016].
 308 Moreover, for every two-fluid / pore network system, a unique locus of energy efficiency
 309 maxima is formed, $r^*(Ca)$. The flow conditions that correspond to the $r^*(Ca)$ locus and
 310 minimize the total energy dissipation per unit of NWP flow-rate, are called *critical flow*
 311 *conditions* (CFCs). The critical energy efficiency index, $f_{EU}^*(Ca)$, and the associated locus
 312 of CFCs, $r^*(Ca)$, provide a strong tool for flow analysis and characterization [Valavanides,
 313 2018(b)].

314 2.4 Universal relative permeability scaling form, incorporating flow-rate dependency

315 The *DeProF* (Decomposition in Prototype Flows) model is a hybrid mechanistic-stochastic
 316 model for predicting the dimensionless macroscopic pressure gradient, x , in immiscible,
 317 steady-state two-phase flows through pore networks. It integrates pore-scale interfacial
 318 dynamics and network-scale cooperative phenomena to estimate the effective conductivity of
 319 different pore unit cell classes in a stochastic approach. Utilizing effective medium theory
 320 and ensuring pore-to-macro-scale consistency for non-wetting and wetting phase mass
 321 transport, *DeProF* formulates an implicit algebraic expression linking x to key system and
 322 flow parameters: capillary number, Ca , flow-rate ratio, r , viscosity ratio, κ , dynamic
 323 advancing and receding contact angles (θ_A, θ_R), and a set of parameters describing pore
 324 network geometrical and topological characteristics. Extensive simulations with the *DeProF*
 325 model algorithm have mapped the flow regime dependencies across five orders of magnitude
 326 in Ca and r , for nine different viscosity ratios [Valavanides, 2018(a)].

327 Based on the *DeProF* simulations it was possible to infer a universal description of the
 328 dependence of the reduced pressure gradient, $x(Ca, r)$, on the capillary number, Ca , and the
 329 flow-rate ratio, r , expressed by the universal scaling form [Valavanides, 2023],

$$x(\log Ca, \log r) = A(\log Ca) + \kappa r \quad (13)$$

330 whereby the effects of capillarity and viscosity are partitioned in two decoupled terms. The
 331 linear term describes the fractional contribution of the bulk viscosities through the viscosity
 332 ratio, κ . The non-linear term, $A(\log Ca)$, is the *Intrinsic Dynamic Capillary Pressure (IDCP)*
 333 function; it accounts the capillarity effects associated to the physicochemical properties of the
 334 two-fluid system and the pore network, i.e. wettability (dynamic receding and advancing
 335 contact angles) and pore network geometry, at different flow conditions. In particular, the
 336 *IDCP* function, $A(\log Ca)$, is a *characteristic property* of the NWP/WP/PM flow system. The
 337 term *dynamic* in IDCP is used to indicate that capillary pressure is evaluated at different flow
 338 conditions – not in static equilibrium [Valavanides, 2023].

339 In the present work, we perform a SCAL study and recover the IDCP function, $A(\log Ca)$,
 340 specific to the two-fluids/pore network systems under consideration.

341 **3 Materials and methods**

342 *3.1 Microfluidic model networks and fluids*

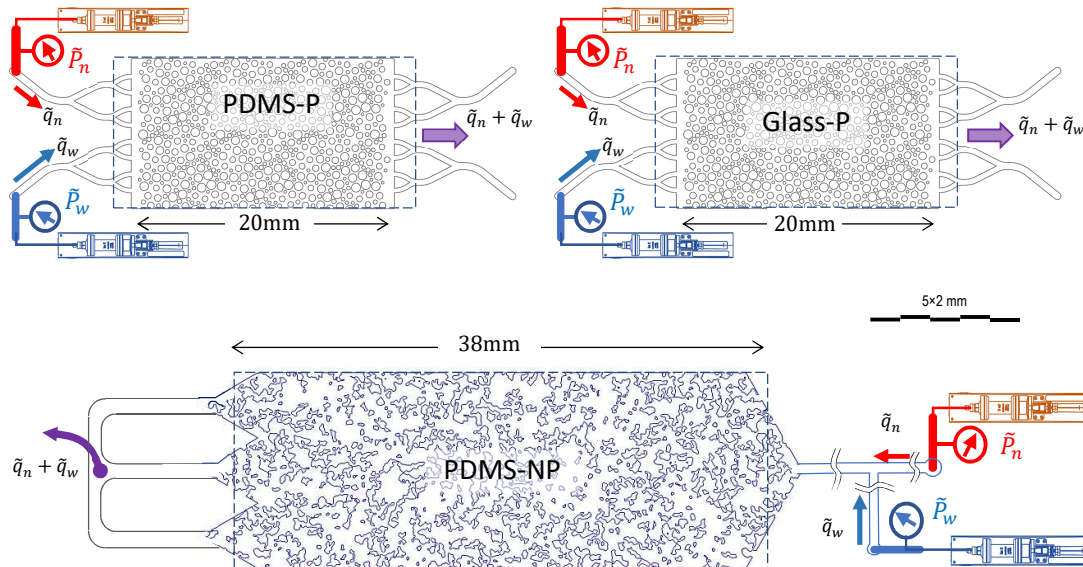
343 Three model pore networks were used in the study. All micromodels are 2,5D planar with a
 344 three-dimensional pore structure. The pore structure of the median plane section of the
 345 micromodels is exhibited in **Figure 2**. Two of the network models have a periodic structure
 346 (see following paragraphs), one is non-periodic. For quick reference, the codification of the
 347 network geometry is “P” for periodic and “NP” for non-periodic.

348 Two of the model pore networks (denoted as PDMS-P and PDMS-NP) were produced
 349 using Poly-Di-Methyl-Siloxane (PDMS) implementing optical and soft lithography
 350 techniques [Xia & Whitesides, 1998; Karadimitriou *et al.*, 2013]. The third model pore
 351 network (denoted as Glass-P) was produced using glass by chemical etching techniques
 352 [Wegner & Christie, 1983; Avraam, *et al.*, 1994].

353 The three model networks are referenced by combining the attributes to the matrix
 354 material and the periodicity characteristics, i.e. PDMS-P, Glass-P and PDMS-NP (**Figure 2**).

355 The pore network in the PDMS-P and Glass-P models is periodic in both principal
 356 orthogonal directions; it is made by tiling-up a basic network element in both directions; 3
 357 periods along the longitudinal axis which is also the superficial flow direction, and 2 periods
 358 across the transverse axis. The pore size range is [75-250] μm , with a mean size equal to 180
 359 μm . That range pertains to the diameters of circles inscribed in the various pores; the latter
 360 comprise the void space between the aforementioned cylindrical pillars (“grains”). Because
 361 of the particular geometric configuration there is no clear /nominal characterization of pore
 362 bodies as “chambers” or “throats”. A conventional dimensional delimiter could be the
 363 average diameter of inscribed circles; any pore with larger nominal diameter could be
 364 considered as chamber, whereas a pore with smaller nominal diameter as throat. As per
 365 connectivity, there are no dead-end pores, apart those residing at the sides of the network –
 366 parallel to the longitudinal flow direction.

367 The PDMS-NP geometry is designed following a standard spectral method, where a matrix of
 368 independently distributed Gaussian random numbers is generated in a 2D regular grid and
 369 transformed into the (spatial) frequency domain using a 2D Fast Fourier Transform (FFT)
 370 (see e.g. Yiotis *et al.*, 2019). A spectral filter, derived from the Fourier transform of the
 371 selected covariance model, is then applied to impose the target spatial correlation. Depending
 372 on the selected model, the resulting structure is controlled by a characteristic correlation
 373 length(s), λ_S , and, where applicable, additional shape or smoothness parameters, which
 374 govern the continuity, roughness, and multi-scale character of the solid phase. The filtered
 375 field is inverse FFT-transformed to real space to obtain spatially correlated values (i.e., a
 376 latent continuous random field). A threshold based on the target porosity, ϕ , is then applied
 377 to classify voxels as solid (1) or void (0) and to thus generate binary pore structure (simulated
 378 porous medium). For this contribution, we employ an exponential spatial correlation kernel
 379 with a correlation length equal to $350\mu\text{m}$. The top-view porosity of the domain is set equal to
 380 $\phi = 0.7$, while the average obstacle size is 0.14mm^2 and the media is 0.027mm^2 .
 381



382

383

384 **Figure 2** Mid-plane section of the microfluidic networks (in-scale) used in the co-
 385 injection experiments and schematics of the syringe pumps. The fluids are co-injected
 386 through the inlet micro-channeling and the immiscible flow is collected at the exit. Top: the
 387 periodic (P) networks made of PDMS and glass; bottom: the non-periodic (NP) network
 388 made of PDMS.

389

390 Due to the different manufacturing processes between the PDMS and Glass networks,
 391 there are differences in the out-of-plane layout of the pore (void) network. Both the PDMS
 392 networks (PDMS-P and PDMS-NP) have an orthogonal geometry. In the PDMS-P network
 393 circles correspond to the planar cross-sections of the PDMS cylinders (solid pillars of circular

394 cross-sections) connecting the two parallel plates confining the flow. In the PDMS-NP
 395 network, the vertical pillars connecting the two horizontal plates (bottom and top) have a
 396 prismatic geometry of irregular cross-section. In that context, any cross-section perpendicular
 397 to the horizontal (mid-) plane in any the two PDMS networks comprises orthogonal sections
 398 of void and solid spaces. The effective, overall dimensions of the PDMS-P network are
 399 10mm×20mm. The depth of the porous structure, in the PDMS-P and PDMS-NP networks is
 400 constant throughout the entire pore space and the surface is smooth. The depth in the Glass-P
 401 network has some degree of irregularity with surface micro-roughness due to the
 402 implemented chemical etching technique. The basic geometric configuration of the three
 403 models is given in **Table 1**.

404

405 **Table 1** Basic geometric configuration of the three model networks used in the study.

Network geometric properties	PDMS-P	Glass-P	PDMS-NP
Length, \tilde{L} [mm]	20	20	38
Width [mm]	10	10	13
Depth [μm]	43	~36	56
Nominal height of chip plate [μm]	54	45	70
Average surface cross-section (void), \tilde{A} [m^2]	4.3×10^{-7}	$\sim 3.5 \times 10^{-7}$	1.4×10^{-7}
Median plane area porosity	0.45	0.45	0.7
Abs. Permeability, \tilde{k} [m^2]	1.18×10^{-11}	0.68×10^{-11}	1.04×10^{-11}

406

407 The absolute permeabilities of the three networks, taking into account the inlet/outlet
 408 micro-channel network, were measured by injecting a single phase and implementing the
 409 saturated flow Darcy expression. Measured values of absolute permeabilities are given in
 410 **Table 1**. Together with the average void surface of the cross section (perpendicular to flow).

411 The two immiscible fluids are injected through the inlet micro-channeling with
 412 predetermined fluxes, \tilde{q}_n, \tilde{q}_w . The immiscible flow exits the network through the outlet
 413 micro-channeling at atmospheric pressure.

414 The fluids used in the experiments were deionized water dyed with ink, and FluorinertTM
 415 FC-770. The basic physicochemical and wettability properties of the fluids are presented in
 416 **Table 2**. The addition of the dye in water has practically no effect on its viscosity and
 417 density, as confirmed by relevant measurements. Note that the wettability of the two fluids
 418 changes with the material of the network matrix (solid phase), i.e. PDMS is hydrophobic and
 419 wetted by the FluorinertTM FC-770, whereas Glass is hydrophilic and wetted by the dyed
 420 water. Wettability of the two-fluid and pore network system is described by the dynamic
 421 advancing, θ_A , and receding, θ_R , contact angles. Nominal values have been roughly
 422 estimated from visual observations of the recorded snapshots.

423

424 **Table 2** Basic physicochemical properties of the proxy fluids used in the study.

Fluids & physicochemical properties	Density	Dynamic viscosity	Interfacial tension	Solid	
	$\tilde{\rho}$ [kg/m ³]	$\tilde{\mu}$ [mPas]	$\tilde{\gamma}_{nw}$ [N/m]	PDMS	Glass
Fluorinert TM FC-770	1793	1.359	55×10^{-3}	WP	NWP
Deionized Water + Dye	1000	1.00		NWP	WP
Advancing cont. angle, θ_A [deg]				54 ± 5	41 ± 3
Receding cont. angle, θ_R [deg]				45 ± 5	35 ± 4

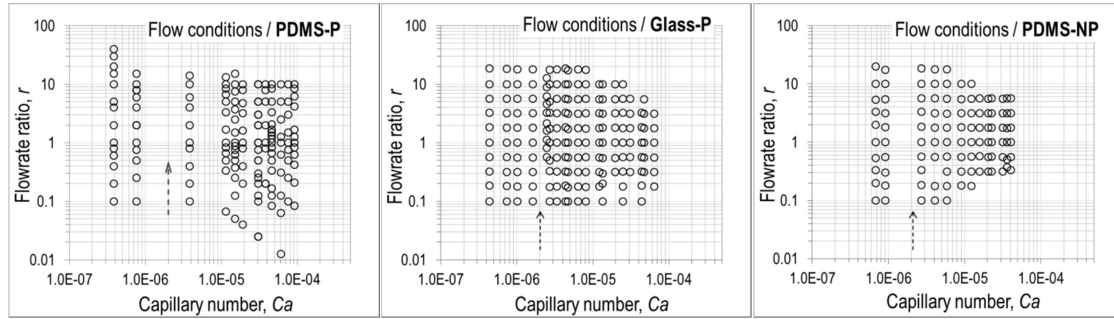
425

426 **3.2 Experimental set-up and procedure**

427 The experimental set-up is identical to that already used in the precursor study using the
428 PDMS-P network [Karadimitriou *et al.*, 2023]. The two fluids were co-injected independently
429 at predetermined volumetric fluxes, using two CETONITM, neMESYS 1000N, DC-motor
430 driven syringe pumps, combined with a BASE120 module. Inlet pressures per phase were
431 measured with a set of ElveflowTM MPS sensors, depending on the values of the expected
432 pressure build-up during the injection and the desirable /acceptable measurement accuracy.
433 Both syringe pumps, and logging of the pressure readout values were controlled with
434 QMixElementsTM. Sampling and recording of the pressure values at the inlet port for each
435 phase was set at rates of 10 Hz. The entire flow system was visualized using an open-air
436 microscope, with a monochromatic camera, BaslerTM 5 Mpx, 23 fps, acA2440-20gm. The
437 purpose of visualizing the interstitial flow was for cross-checking between the structure of the
438 flow, the read-outs from the pressure transducers, and the injected fluxes, in order to trace
439 when the interstitial flow has reached steady-state (see procedure cycle steps in the following
440 paragraph). Snapshots of the interstitial flow structure were captured at frame rates between
441 15 and 1 Hz, depending on flow conditions. The resolution was set at 8 μ m/pixel, adequate to
442 observe pore-scale events.

443 The procedure followed for each *experiment* included a complete cycle of co-injecting the
444 two phases at constant WP volumetric flow-rate, but with successive increases of the NWP
445 flow-rate. The protocol followed was identical for all experiments in the three model
446 networks as in the precursor study [Karadimitriou *et al.*, 2023]. For every *i*-experiment a
447 fixed capillary number value, Ca_i , is maintained, whereas the flow-rate ratio takes successive
448 *j*-step-up values, r_j . The domain of flow conditions covered in the experiments is depicted in
449 **Figure 3**. A total of 44 constant- Ca experiments were performed; 13 in the PDMS-P
450 ($i = \{1, \dots, 13\}$), 19 in the Glass-P ($i = \{1, \dots, 19\}$), and 12 in the PDMS-NP ($i = \{1, \dots, 12\}$),
451 model networks, covering a range of 3 \times 3 orders of magnitude on Ca and r values.

452



453

454 **Figure 3** The domains of steady-state flow conditions examined in the study. Markers
 455 indicate values of the capillary number, Ca_i , and flow-rate ratio, r_j . The dashed arrow
 456 indicates the direction of increase of the flow-rate of the NWP (at fixed Ca_i) for all
 457 experiments.

458

459 The typical cycle in every i -experiment comprises the following steps:

460

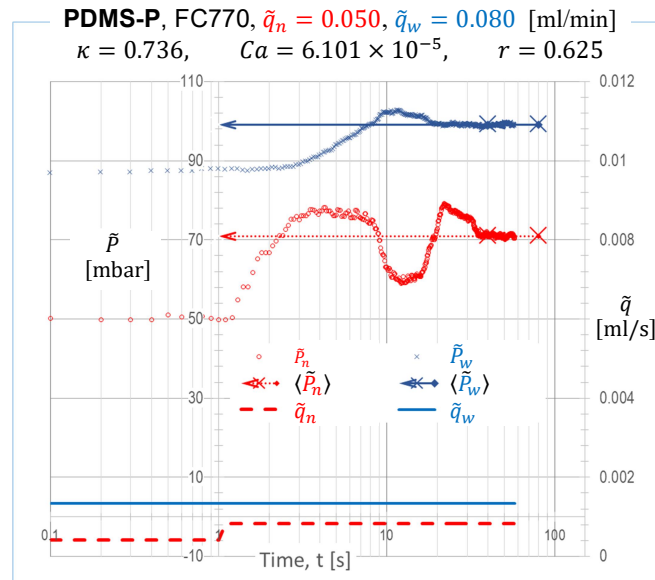
- 461 1. The micromodel is initially fully saturated with the WP.
- 462 2. The WP is injected at a fixed volumetric flow-rate in order to maintain a constant
 463 value of the capillary number, Ca_i , during the entire cycle of the experiment.
- 464 3. The volumetric flow rate of the non-wetting phase (NWP) is initially set to
 465 approximately one-tenth of that of the wetting phase (WP). It is then increased in
 466 successive steps (approximately 9–12 increments). After each incremental increase in
 467 the NWP flow rate, sufficient time is allowed for the interstitial flow to attain steady-
 468 state conditions. Steady state is identified when the time-averaged pressures of both
 469 phases exhibit kinetic stabilization, characterized by small oscillations around
 470 constant mean values (**Figure 4**). Subsequently, the interstitial flow is visually
 471 evaluated in terms of saturation and pore-scale dynamics to confirm stabilization or to
 472 verify that any remaining fluctuations follow a consistent, short-period cycle.
 473 Following this assessment, the volumetric flow rate of the NWP is further increased in
 474 a stepwise manner.
- 475 4. After successive repeats with progressive stepwise increments of the flow-rate of the
 476 NWP, until a flow-rate ratio value $r \geq 10$ is reached, the experiment for that constant-
 477 Ca value stops.
- 478 5. The system is then reconfigured and a new cycle is deployed pertaining to a new Ca
 479 value.

479 3.3 Data logging and management

480 For each run at constant \tilde{q}_n and \tilde{q}_w the values of flow-rates and gauge pressures at the inlet
 481 ports for each phase, were sampled and recorded (as described in 3.2). A typical evolution of
 482 the two flow-rates and pressures at the inlet ports is depicted in the diagram in **Figure 4**.
 483 Please note that, the time axis (horizontal) and the flux axis (vertical, right) are logarithmic

484 whereas the pressure axis (vertical, left) is linear.

485



486

487 **Figure 4** Typical, time evolution of the inlet pressures (circle and cross markers, left
 488 axis) for a typical co-injection of the two phases at predetermined volumetric flow-rates
 489 (dashed lines, right axis). The two arrows indicate the time averaged pressures when the flow
 490 has reached steady-state. Please refer to the main text for details.

491

492 Pressure values are indicated by markers; flow-rates are indicated by lines. In particular,
 493 pressure values measured at the inlet port are indicated by the small circle markers (red, ○)
 494 for the NWP and by the small cross markers (blue, ×) for the WP. The compact line (blue, —
 495) indicates the volumetric flow-rate for the WP, \tilde{q}_w , and the dashed line (red, - - -) for the
 496 NWP, \tilde{q}_n . The step in the NWP line indicates the imposed increase in volumetric flow-rate
 497 succeeding the previous co-injection set-up. The long horizontal arrows, pointing to the
 498 pressure axis on the left, indicate the average pressure values, or “endpoint pressure values”,
 499 calculated when interstitial steady-state conditions settle-in. Time-averaging is taken over the
 500 time interval delimited by the two pairs of large crosses over a selected interval, delimited by
 501 the two cross markers (×), red for the NWP and blue for the WP pressures. Delimiting this
 502 time interval for every examined flow set-up, (Ca, r) , follows after identifying some form of
 503 stabilization in the corresponding pressure log diagram. Then, the average (endpoint)
 504 pressures, $\langle \tilde{P}_n \rangle, \langle \tilde{P}_w \rangle$, are automatically calculated. Finally, the pressure gradients for the WP
 505 and the NWP are then readily calculated as

$$(\Delta \tilde{p} / \Delta \tilde{z})_i = \langle \tilde{p}_i \rangle / L, \quad i = n, w \quad (14)$$

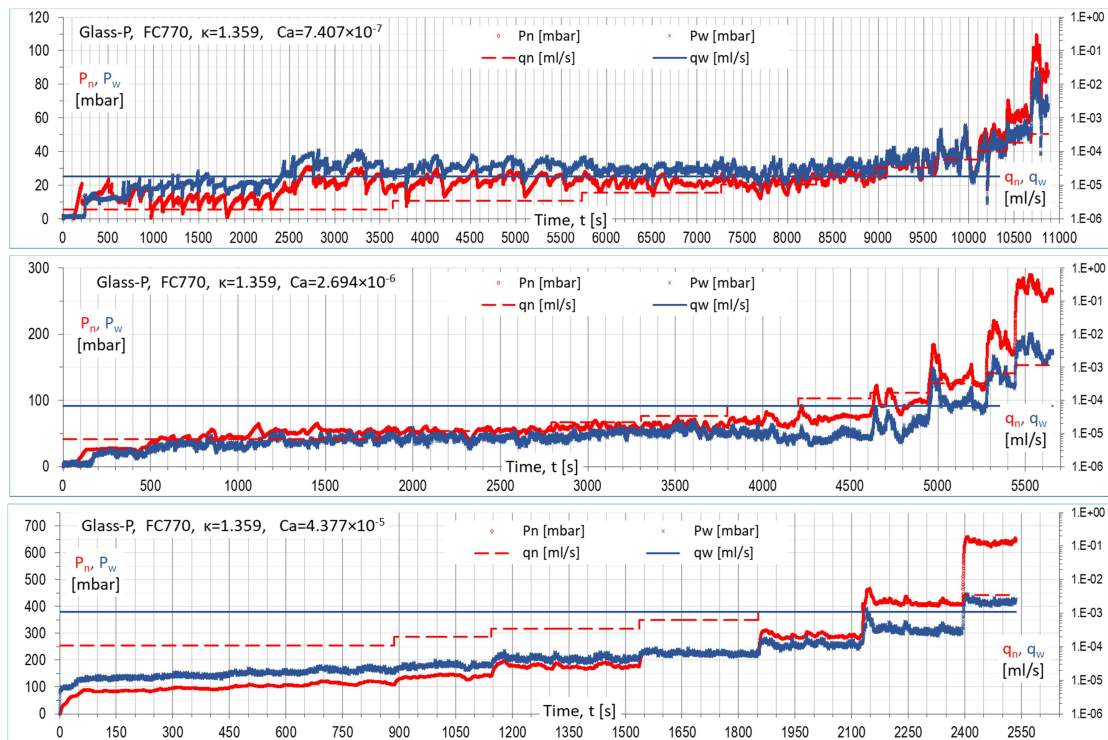
506

507 Typical, time evolution diagrams, pertaining to entire cycles of constant- Ca experiments
 in the Glass-P network, are also presented in **Figure 5**. Again, the measured pressures at the

508 inlet ports are indicated by the small circle markers (red, ○) for the NWP, and by the small
 509 cross markers (blue, ×) for the WP. The compact line (blue, —) indicates the WP
 510 volumetric flow rate, \tilde{q}_w , dashed line (red, - -) for the NWP, \tilde{q}_n . Please note, the time scale
 511 is now linear. As in the diagram in **Figure 4**, we may observe a time delay until quasi steady-
 512 state conditions settle in after each flow rate step-up.

513 We may also observe that the magnitude of the pressure fluctuations, as well as the time
 514 delay and the minimization of the associated fluctuations, depend on the imposed co-injection
 515 flow rates, i.e. the (Ca, r) values. In the three diagrams in **Figure 5**, starting from a low
 516 capillary flow at $Ca = 7.407 \times 10^{-7}$ (top diagram) and moving to intermediate,
 517 capillary/viscous, at $Ca = 2.694 \times 10^{-6}$ (middle), and then to viscous flow, at $Ca =$
 518 4.377×10^{-5} (bottom), we may observe an (expected) systematic progressive decrease of
 519 the aforementioned time delay accompanied by a similar decrease in the magnitude of
 520 pressure fluctuations around the endpoint pressure average.

521



522

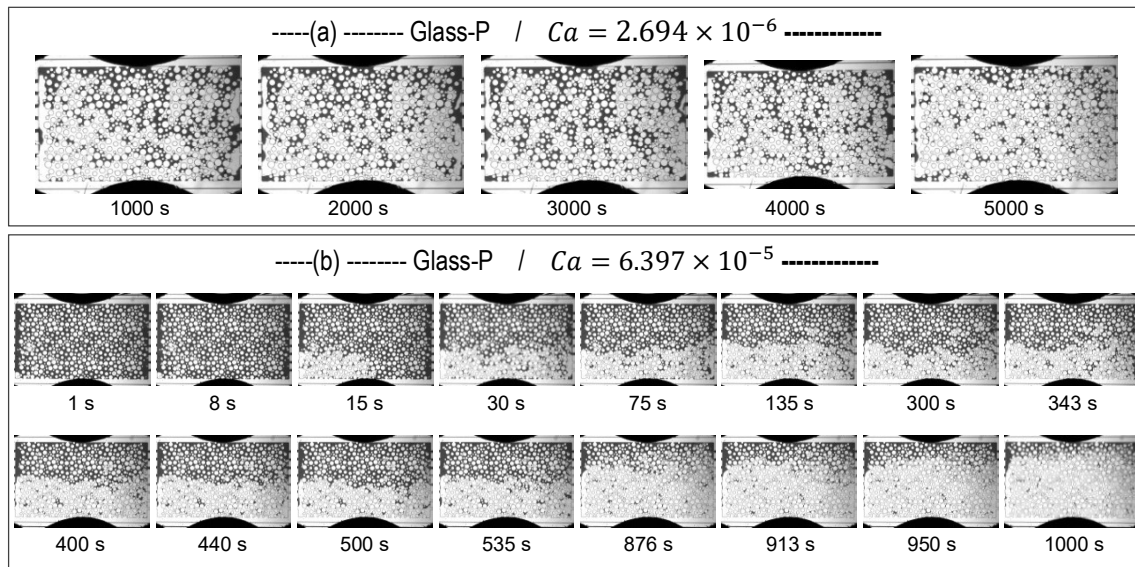
523 **Figure 5** Typical, time evolution diagrams pertaining to experiments of steady-state co-
 524 injection at 3 different Ca in the Glass-P network. The measured pressures at the inlet ports
 525 are indicated by the small circle markers (red, ○) for the NWP, and by the small cross
 526 markers (blue, ×) for the WP. The compact line (blue, —) indicates the WP volumetric flow
 527 rate, \tilde{q}_w dashed line (red, - -) for the NWP, \tilde{q}_n .

528

529 The characterizations “capillary”, “capillary/viscous” and “viscous” are not arbitrary; they
 530 can be confirmed by referring to the compound diagrams in **Figure 11** whereby the afore

531 referenced Ca values are traced in the initial phase, the growth phase (sharp upward slope in
 532 the middle) and the plateau phase (flattening-out) of the sigmoid curves delineating the
 533 maximum values of the energy efficiency of the process (section 4.2). A similar trend can be
 534 observed between the successive increments in the flow-rate ratio for every constant- Ca
 535 experiment. Albeit spanning over different regions in the Ca domain, this decay trend is
 536 systematic for all the systems examined (PDMS-P, Glass-P and PDMS-NP). It is an
 537 indication of flow hysteresis associated with geometrical/topological reconfiguration of the
 538 flow structure of the disconnected NWP until a local energy minimum is reached [Cueto-
 539 Felgueroso & Juanes, 2016; Rucker *et al.*, 2021].

540 Indicative snapshots of the interstitial flow structure evolution are presented in **Figure 6**
 541 for two co-injection experiments at $Ca = 2.694 \times 10^{-6}$ and $Ca = 6.397 \times 10^{-5}$ in the
 542 Glass-P model network. The WP (Deionized Water + Dye) is black, and the NWP
 543 (FluorinertTM FC-770) is transparent (“white”).
 544



545
 546

547 **Figure 6** Selected snapshots from steady-state co-injections, Glass-P network. WP is
 548 black, NWP is transparent. Flow direction is from left to right. Numbers indicate time lapse
 549 from injection start. (a) $Ca = 2.694 \times 10^{-6}$ (140-5000 s) (b) $Ca = 6.397 \times 10^{-5}$ (1-1000 s).

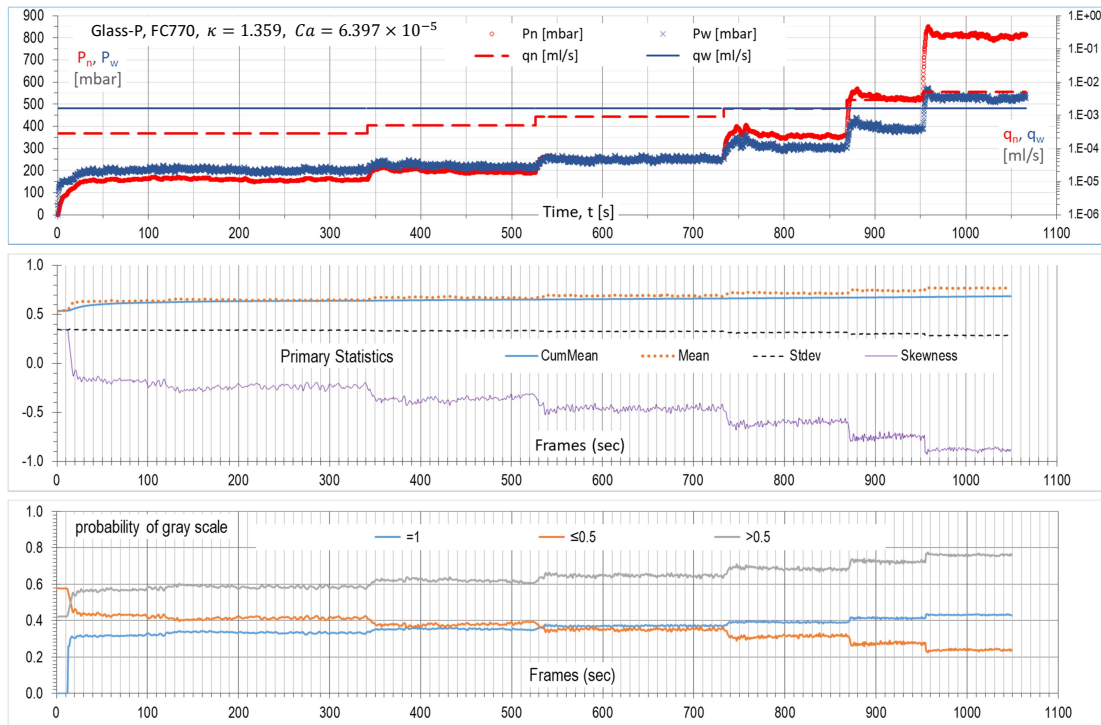
550

551 The flow segregation observed in the snapshots in **Figure 6(b)**, pertains to WP injection at
 552 high Ca values. The fraction of segregation, between the WP (black) and NWP (transparent),
 553 increases with increasing flow-rate ratio. The snapshots on the 1st row in **Figure 6(b)**, record
 554 the initial moments of co-injection of the NWP with flow rate ratio $r = 1.7/9.5 = 0.18$;
 555 while those on the 2nd row indicate the flow structure during the successive flow-rate step-
 556 ups. Flow segregation may be attributed to poor flow mixing downstream the two inlet ports
 557 as well as, self-structuring of the interstitial flow to adapt to the entry flow (initial)

558 conditions. The latter is compatible with reduction of energy dissipation for the imposed flow
 559 conditions at high Ca and moderate to high r values. Flow mixing by disconnection of the
 560 NWP creates menisci, these increase pressure gradients and, consequently, energy dissipation
 561 increases.

562 In the same context, in an effort to correlate the evolution of the interstitial flow structure
 563 with the evolution of the pressures, we calculated the primary statistics (mean, cumulative
 564 mean, standard-deviation, skewness) and selected probabilities of the grayscale intensity for
 565 each recorded frame and for a variety of flow conditions at different networks. A typical time
 566 evolution of the aforementioned grayscale intensity primary statistics is presented in **Figure**
 567 **7**. The diagrams pertain to the flowrate ratio co-injections within the Glass-P model network
 568 at $Ca = 6.397 \times 10^{-5}$. In that figure, the time evolution of the measured pressures (top
 569 diagram) is exhibited against the evolution of primary statistics (middle diagram) and
 570 selected probabilities of the grayscale intensity (bottom diagram).

571



572

573 **Figure 7** Direct comparison of time evolution diagrams pertaining to the entire
 574 experiment of steady-state co-injection at $Ca = 6.397 \times 10^{-5}$ in the Glass-P model network.
 575 **Top** – Pressure values measured at the inlet port, similar to diagrams presented in **Figure 5**.
 576 **Middle** –Time evolution of the grayscale intensity primary statistics (mean, cumulative
 577 mean, standard-deviation, skewness) for each recorded frame pertaining to the entire
 578 network. **Bottom** – Selected probabilities of the grayscale intensity for each recorded frame.

579

580 The above statistics show when in the timeline a steady-state has been reached for each

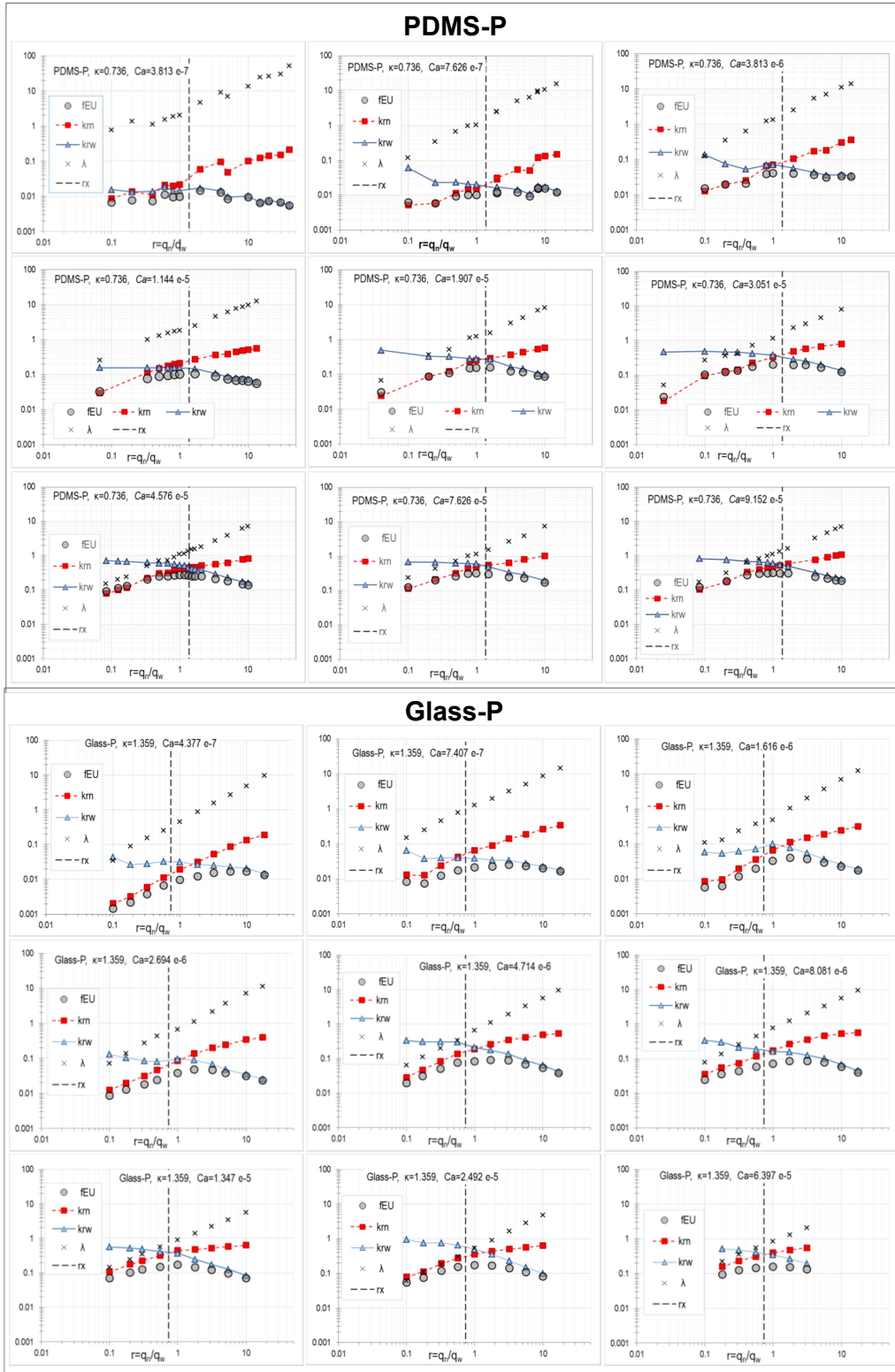
581 flowrate bump-up under constant- Ca . The most significant index among the primary statistics
 582 seems to be the skewness coefficient (and the probability of grayscale intensity at 0.5, i.e.
 583 exactly between black and white color intensities), which is more sensitive compared to the
 584 mean and the standard-deviation for this type of experiment.

585 4 Results

586 The pair of pressure gradient values, $\{(\Delta\tilde{p}/\Delta\tilde{z})_n, (\Delta\tilde{p}/\Delta\tilde{z})_w\}$, was used to calculate the
 587 corresponding pair of relative permeability values for the NWP and WP, $\{k_{rn}, k_{rw}\}$, from eqn
 588 (7). We need to stress here that we have considered the general condition that the flow may
 589 not be fully developed, therefore the NWP and WP pressure gradients would not be
 590 necessarily equal. In such general condition, $(\Delta\tilde{p}/\Delta\tilde{z})_n \neq (\Delta\tilde{p}/\Delta\tilde{z})_w$; therefore, the pairs of
 591 NWP and WP relative permeability values, $\{k_{rn}, k_{rw}\}$, were calculated using eqn (15)

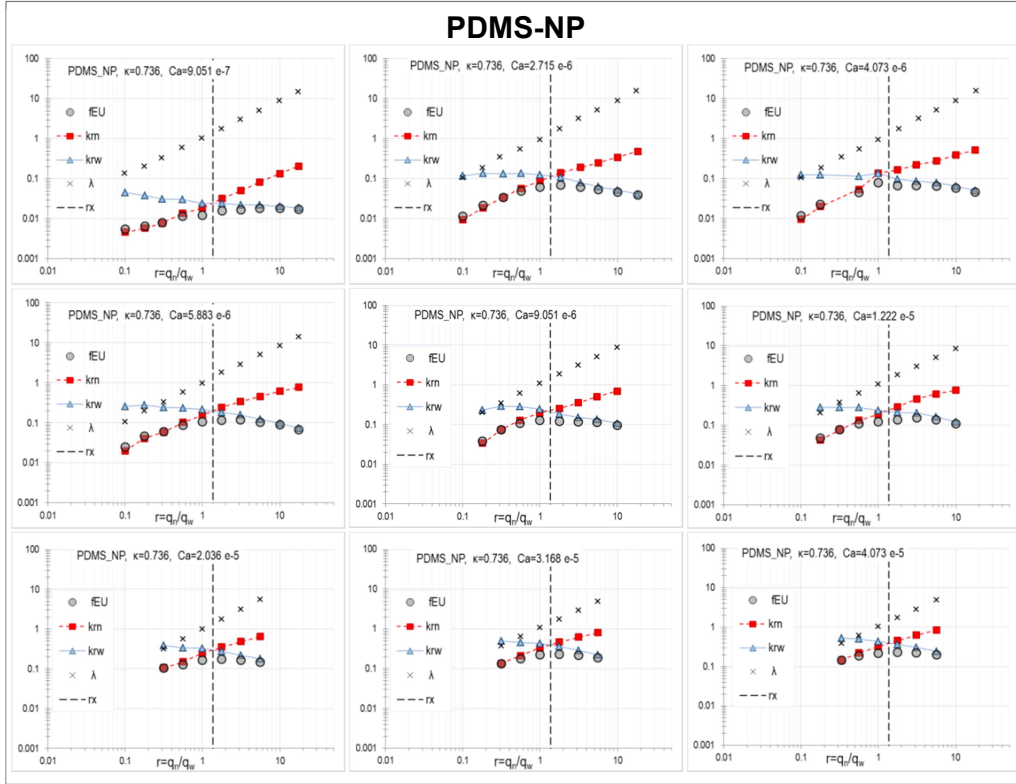
$$k_{rn} = \frac{\tilde{\mu}_n \tilde{U}_n}{\tilde{k} \left(\frac{\Delta\tilde{p}}{\Delta\tilde{z}} \right)_n}, \quad k_{rw} = \frac{\tilde{\mu}_w \tilde{U}_w}{\tilde{k} \left(\frac{\Delta\tilde{p}}{\Delta\tilde{z}} \right)_w} \quad (15)$$

592 The collected relative permeability values per constant- Ca experiment were plotted
 593 against the corresponding values of the flow-rate ratio, r , together with the corresponding
 594 values of energy efficiency, f_{EU} , eqn (19), and mobility ratio, λ , eqn (3). A total of 44
 595 diagrams each per constant- Ca experiment are plotted. Due to space limitations
 596 representative diagrams spanning the entire region of constant- Ca experiments are presented
 597 in **Figure 8**.
 598



599

600



601
602

603 **Figure 8** Indicative diagrams of relative permeability for the NWP and WP (k_{rn} , ■, and
604 k_{rw} , ▲), energy efficiency, f_{EU} (○), and mobility ratio, λ (×) in terms of flow-rate ratio, r . The
605 diagrams are grouped according to network type. Within each group, diagrams are arranged
606 in order of increasing capillary number, Ca , progressing from left to right and from the top to
607 the bottom row. Each diagram corresponds to a constant- Ca experiment. The vertical dashed
608 lines denote the cross-over flow-rate ratios for relative permeability, as predicted by eqn (11).
609

610 *4.1 Relative permeability scaling incorporating flow-rate dependency logging and*
611 *management*

612 We proceed with revealing the flow dependent, relative permeability scaling for the steady-
613 state two-phase co-injections in the three microfluidic pore networks.

614 Considering the flow is fully developed, we calculated the reduced pressure gradient,
615 $x = 1/k_{rw}$, i.e. the inverse of the relative permeability of the WP using eqn (8). The entire
616 set of x values is plotted in terms of the flow-rate ratio, r , in the top-row diagrams and in
617 terms of the capillary number, Ca , in the bottom-row diagrams in **Figure 9**.

618 In particular, the values of reduced pressure gradient, x , are displayed in terms of $\log r$, in
619 groups of constant- Ca values. Note that with increasing r , there is an obviously systematic,
620 asymptotic trend in aligning to the dashed, inclined line towards a virtually decoupled flow
621 state. That is described by

$$\text{As } r \rightarrow \infty, \log x = \log \kappa + \log r \Leftrightarrow x = \kappa r \quad (16)$$

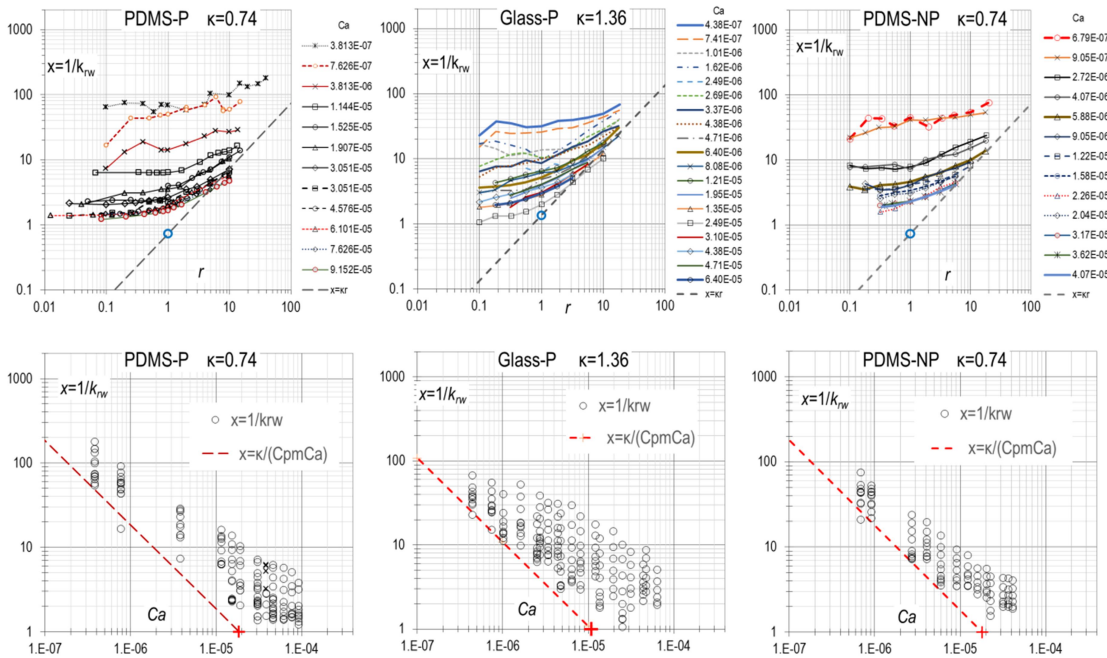
622 The inclination of the dashed line in the three log-log, top-row diagrams in **Figure 9**, is
 623 equal to 1: 1, and its pivot (marked by \circ) is located at $\{1, \kappa\}$.

624 In the bottom-row diagrams in **Figure 9**, the values of reduced pressure gradient, x , are
 625 displayed in terms of $\log Ca$, and lined-up in vertical rows of constant Ca . Within the same
 626 row, markers depict different values of the flow-rate ratio, r . As not all experiments were run
 627 on the same flow-rate ratio values, it is not possible to group the x -values into r -classes.

628 Again here, we may observe the tendency (a confluence) of the markers to converge and
 629 align – in an asymptotic manner – towards the inclined, dashed line (in red). The trend is
 630 described by

$$\begin{aligned} \log Ca \ll 0, \log x = \log \kappa - \log C_{pm} - \log Ca \Leftrightarrow x = \kappa / (C_{pm} Ca) \\ = 1 / (Ca_{pm} Ca) \end{aligned} \quad (17)$$

631



632

633

634 **Figure 9** Reduced pressure gradient (inverse WP relative permeability) values in terms
 635 of r for constant Ca values (top row), and reduced pressure gradient values in terms of Ca for
 636 different r values (bottom row), for the three NWP/WP/PM systems examined in the study
 637 (periodic networks PDMS-P, left column, Glass-P, center column, and non-periodic networks
 638 PDMS-NP, right column).

639

640 The functional form of this asymptote is given by an expression, up to a constant value,

641 C_{pm} , associated to the NWP/WP/PM system [Valavanides, 2023]. The line asymptote has a
 642 negative inclination with slope equal to -1. For the available set of data displayed in the
 643 bottom row diagrams, we have used arbitrary, best-guess, constant values $\log C_{pm}$, to pivot
 644 the line along the Ca axis at $Ca_{pm} = \kappa/C_{pm}$. The pivot is indicated by the thick red cross
 645 marker (+) in each diagram. By increasing these values but keeping the negative inclination
 646 equal to 1: 1, the dashed lines (asymptotes) are transferred in parallel to the left, at lower Ca
 647 pivot points, and vice versa. The “best guess” values used to pivot the asymptotes in the
 648 diagrams do not have an effect on the following. To estimate the C_{pm} values more precisely,
 649 we need to have more data and, most importantly, the data should pertain to capillarity
 650 dominated flows, i.e. to flows at low Ca values, close to the confluence region of the data
 651 markers. The recovery of the correct C_{pm} value for a certain system is essentially a “dynamic
 652 network-typing” procedure. That is because the value of C_{pm} is associated to the interaction
 653 between the structure of the pore network and the wettability of the two-fluid system – the
 654 dynamic advancing and receding contact angles and the associated dynamic hysteresis.

655 The trend in the diagrams in **Figure 10** is similar to the trend observed in the *DeProF*
 656 model simulations [Valavanides, 2023] pertaining to a virtual sandstone network model. The
 657 same trend is observed in a similar diagram, pertaining to the lab study on a natural sandstone
 658 core [Valavanides et al., 2020]. Recall that the inclined asymptotes describe or delineate the
 659 domain of flow conditions whereby the compound flow resistance, attributed entirely to the
 660 bulk phase viscosities, is partitioned on complementary volume fraction ratios, namely,
 661 saturation. And it is only at those high flow-rate conditions (high- Ca) that relative
 662 permeabilities can be expressed in terms of saturation in a “saturation-dependency” fashion.
 663 Similar observations have been reported by Chevalier et al. (2015) albeit for the case of
 664 desaturation curves, i.e. when the WP is sweeping the NWP. A similar trend is observed in
 665 the very low- Ca regime (capillarity dominated flows); nevertheless that trend is a bit fuzzy as
 666 it depends strongly on the distribution of the menisci of the stranded ganglia within the
 667 network. That, on its turn, indicates history dependence.

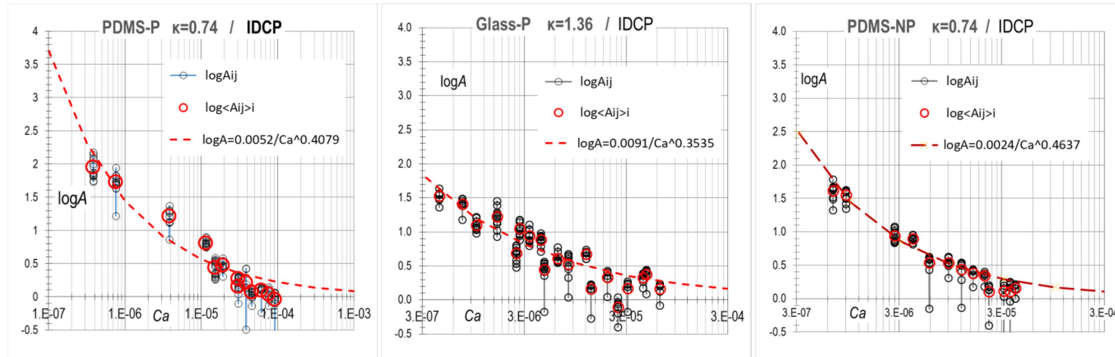
668 In order to describe the steady-state two-phase flow in the particular microfluidic system,
 669 in the form of the universal scaling function eqn (13), we need to reveal the associated kernel
 670 function, $A(\log Ca)$, namely the *Intrinsic Dynamic Capillary Pressure* (IDCP) curve
 671 [Valavanides, 2023]. In essence, the IDCP represents the contribution of the capillary
 672 resistances within the overall flow resistance in any particular two-fluid and pore network
 673 flow system –hence the adjectives “intrinsic” and “dynamic”. To reveal the IDCP for each
 674 examined system we have implemented the fitting procedure described in [Karadimitriou et
 675 al., 2023].

676 In the diagrams in **Figure 10**, we plot the A_i values calculated in terms of Ca_i , via eqn
 677 (13). The small black circles mark the IDCP values, A_{ij} , per r_j , aligned into rows of constant-
 678 Ca_i groups. Average values of $A_i = \langle A_{ij} \rangle$ per constant- Ca_i are marked with large red circles.
 679 These are fitted by a power law (red dashed curve),

$$\log A = aCa^{-b} \tag{18}$$

680 The power law indicates that, asymptotically, as $Ca \rightarrow \infty$, $A(\log Ca)$ decays to 1, therefore
 681 eqn (13) becomes $x \rightarrow 1 + \kappa r$, and the saturation dependency is recovered, yet in an
 682 asymptotic fashion, for the viscous flow regime. The values of the fitting coefficients a, b are
 683 exhibited in **Table 3**. Optionally, the standard deviations of the A_{ij} , values per constant- Ca_i ,
 684 can be weighted-in to the square of errors to improve the power law fitting.

685



686

687 **Figure 10** Intrinsic Dynamic Capillary Pressure function, $A(Ca)$, eqn (13), in terms of
 688 the capillary number Ca .

689

690 **Table 3** Power law fitting coefficients of the IDCP curve for the 3 two-fluid/network
 691 systems examined in the study.

Fitting Coefficients, eqn (18) $\log A = aCa^{-b}$	PDMS-P	Glass-P	PDMS-NP
a	0.0052	0.0091	0.0024
b	0.4079	0.3535	0.4637

692

693 4.2 Energy efficiency & critical flow conditions

694 Energy efficiency analysis is a complementary method to reveal latent systematic trends and
 695 get a better image of the interstitial flow structure within the two-fluid/pore network systems
 696 examined in the study. Moreover, it can be used to identify characteristic differences in the
 697 three examined flow systems.

698 We have calculated the energy efficiency index values using the nominal expression, eqn
 699 (12), but instead using the flow-rate ratio, we used the mobility ratio, λ , therefore,

$$f_{EU} = \frac{\lambda k_{rw}}{\lambda + 1} \tag{19}$$

700 In that context, the interstitial flow was described by the *kinetic* [eqn (19)] rather than the
 701 *kinematic* [eqn (12)] definition of the energy efficiency index.

702 The compound diagrams in **Figure 11** provide the results of the energy efficiency
 703 analysis, implementing eqn (19), In particular, the diagrams in **Figure 11**, display two sets of
 704 data.

705 Focusing on the lower part of the diagrams in **Figure 11**, sets of small, light grey circles
 706 indicate the values of energy efficiency, $\{r_j, f_{EU,ij}\}$ per constant- Ca_i experiment (with
 707 reference to the collection of diagrams in **Figure 8**).

708 For every constant- Ca_i experiment, a maximum value is detected from the energy
 709 efficiency values, $f_{EU,ij}$, as

$$f_{EU,i}^* = f_{EU}^*(Ca_i) = \max_j \{f_{EU,ij}, Ca_i\} \quad (20)$$

710 These maximum values are marked by larger, dark grey circles. A remarkably smooth
 711 increase of the maximum energy efficiency values, f_{EU}^* , with increasing Ca , is observed.
 712 Moreover, depending on the flow conditions, the maximum energy efficiency of the process
 713 may increase by 2 orders of magnitude. Operation-wise, that is a quite important
 714 characteristic when designing this type of processes. The maximum values (filled circle
 715 markers) tend to reach a maximum value – the, so called, “ceiling of efficiency”
 716 [Valavanides, 2018(b)], that is given by

$$f_{EU\infty}^* = (1 + \sqrt{\kappa})^{-2} \quad (21)$$

717 The f_{EU} values are marked on the $\log f_{EU}$ diagrams using small grey circles for the energy
 718 efficiency at different capillary number and flow-rate ratios $f_{EU}(Ca_i, r_j)$, and larger dark grey
 719 circles for the maximum values of energy efficiency at every capillary number, Ca_i .

720 The markers indicating the maximum efficiency values, $f_{EU}^*(Ca_i)$, have been fitted by a 4
 721 parameter sigmoid-curve, $f_{EU}^*(Ca)$

$$\log f_{EU}^*(Ca) = \log f_{EU\infty}^* + \frac{\log f_{EU0}^* - \log f_{EU\infty}^*}{1 + \exp[(\log Ca - \log Ca_m)/s_m]} \quad (22)$$

722 where:

723 $f_{EU\infty}^*$ is the global maximum of the energy efficiency attained at the viscous (very high
 724 Ca) regime (the “ceiling” of the system’s efficiency)

725 f_{EU0}^* is the energy efficiency at the capillary (very low Ca) regime,

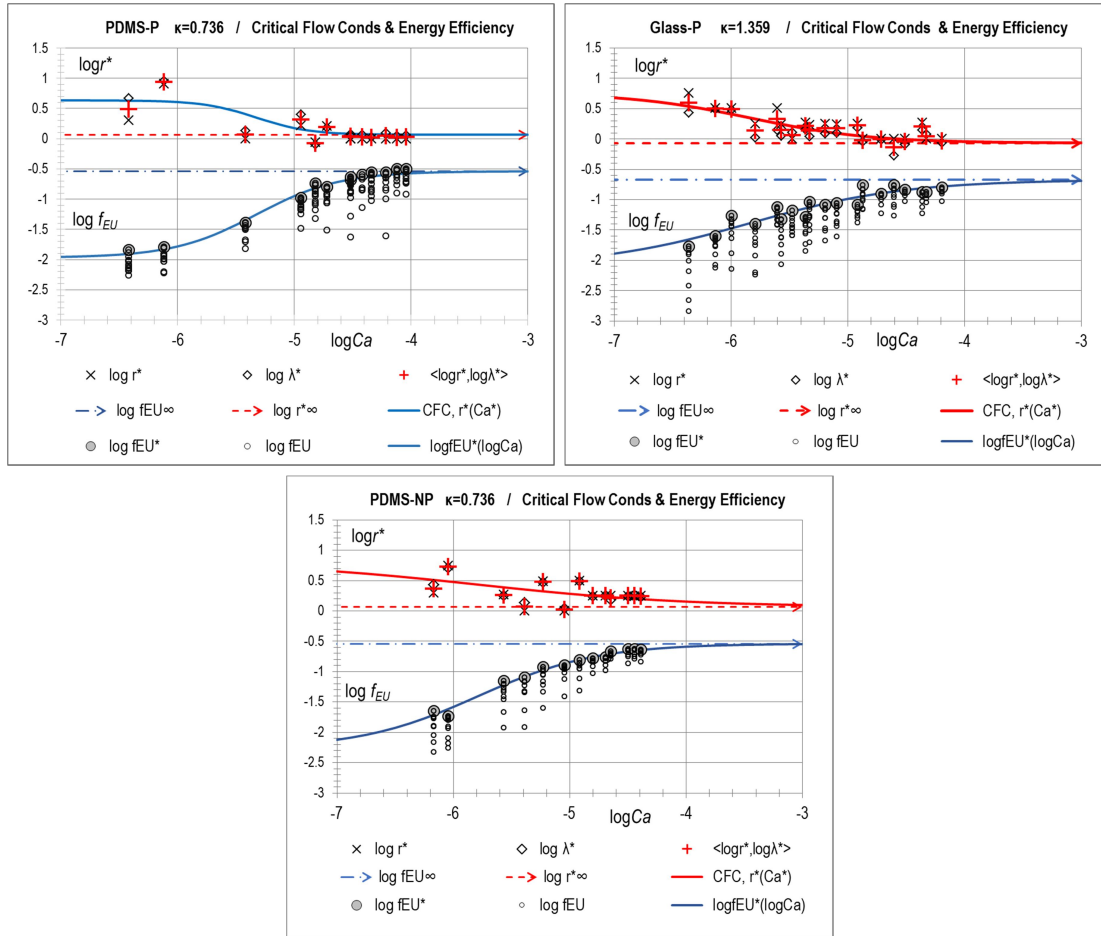
726 These values delineate the two parallel asymptotic boundaries of the S-curve;

727 $\log Ca_m$ is the $\log Ca$ value for the $f_{EU}^*(Ca)$ curve point that is midway between $\log r_0^*$ and
 728 $\log r_\infty^*$;

729 s_m is the corresponding inclination of the curve.

730 The calculated values of the fitting parameters are presented in **Table 4**.

731



732

733

734 **Figure 11** Energy efficiency values $\{r_j, f_{EU,ij}\}$, \circ , and detected maximum values
 735 $\{Ca_i, f_{EU,i}^*\}$, \circ , for the three systems examined in the study (PDMS-P, Glass-P and PDMS-
 736 NP). The corresponding critical flow-rate ratio values, $\{Ca_i, r_i^*\}$, \times , and mobility ratio values,
 737 $\{Ca_i, \lambda_i^*\}$, \diamond , define the so-called Critical Flow Conditions (CFC); upright cross markers in
 738 red, +, indicate the mean of the flow-rate ratio and mobility ratio values, \hat{r}^* , eqn (23).

739

740 Refocusing on the upper part of the of the compound diagrams in **Figure 11**, sets of
 741 markers indicate the critical flow conditions (CFCs), identified by observing the maximum
 742 values of the energy efficiency $f_{EU,i}^* = f_{EU}(Ca_i)$, eqn (20), as evaluated by eqn (19). Both
 743 critical flow-rate ratio, r_i^* , and mobility ratio, λ_i^* , are plotted in terms of $\log Ca$. A
 744 discrepancy between r_i^* and λ_i^* , is pronounced in the low- Ca domain, i.e. at capillarity-
 745 dominated flow regimes, while it is insignificant at the high- Ca domain where bulk viscosity
 746 prevails and the effect of menisci is practically negligible. The detected CFCs show a trend
 747 similar to a sigmoid curve. As the trend is a bit fuzzy in the low- Ca regime, the log-averaged
 748 values were calculated as

$$\log \hat{r}^* = (\log r^* + \log \lambda^*)/2 \Rightarrow \hat{r}^* = \sqrt{r^* \lambda^*} \quad (23)$$

749 These values are marked on the CFC diagrams using red, upright cross markers (+).
 750 Similarly to the energy efficiency maxima, the CFCs markers can be fitted by a 4 parameter
 751 sigmoid-curve

$$\log \hat{r}^* = \log r_\infty^* + \frac{\log r_0^* - \log r_\infty^*}{1 + \exp[(\log Ca - \log Ca_m)/s_m]} \quad (24)$$

752 where:

753 $\log r_\infty^*$ and r_0^* are the critical flow-rate values at the viscous (very high Ca) and capillary
 754 (very low Ca) regimes respectively, and form the two parallel asymptotic boundaries of the
 755 S-curve;

756 $\log Ca_m$ is the $\log Ca$ value for the curve point that is midway between $\log r_0^*$ and $\log r_\infty^*$;

757 s_m is the corresponding inclination of the curve.

758 On the diagrams in **Figure 11**, the dashed red, horizontal line indicates the nominal value
 759 of the critical flow-rate ratio for pure viscous flow conditions (as $Ca \rightarrow \infty$). Given the
 760 viscosity ratio of the two fluids, κ , the theoretical (nominal) value of the critical flow-rate
 761 ratio for pure viscous flow conditions [Valavanides 2018(a)] is estimated as

$$r_\infty^* = 1/\sqrt{\kappa} \quad (25)$$

762 The actual value attained within the lower part of the sigmoid-curves, pertaining to larger
 763 Ca values, indicates an asymptotic trend, that is remarkably close to the theoretically
 764 predicted value, r_∞^* , eqn (25). Moving on to the low- Ca regime (capillary flows) the observed
 765 fuzziness in locating the CFCs is attributed to significant capillary end effects.

766 The parameter values for the sigmoid-curves fitting the energy efficiency maxima and the
 767 CFCs, presented in **Table 4**, are estimated by minimizing the sum of the squared fitting
 768 errors. Comparing the sigmoid-curves for the CFCs in the two-fluid/pore network systems
 769 examined (ref. **Figure 11** & **Table 4**) we observe that the transition from capillary to viscous
 770 flow is smoother (over a broader Ca region) in the PDMS-NP system ($s_m|_{Glass-P} <$
 771 $s_m|_{PDMS-NP}$) and the shift takes place at a larger Ca value
 772 ($\log Ca_m|_{Glass-P} < \log Ca_m|_{PDMS-}$). Overall, the trend across the three two-fluid/pore
 773 network systems examined is systematic. There are conceptual similarities to the diagrams
 774 furnished in the theoretical framework [Valavanides, 2018(b)], and also to the diagrams
 775 produced in the SCAL study by the IFP group [Valavanides *et al.*, 2020] on a natural core
 776 (Clashach sandstone) across a broad domain of flow conditions.

777

778 **Table 4** Characteristic parameter values for the three two-fluid/pore network systems
 779 examined in the study.

780

Parameter	PDMS-P	Glass-P	PDMS-NP
Maximum energy efficiency, $f_{EU}^*(Ca)$, eqn (22)			
$\log f_{EU\infty}^*$	-0.538	-0.671	-0.538
$\log f_{EU0}^*$	-1.968	-2.100	-1.732
s_m	0.355	0.663	0.510
$\log Ca_m$	-5.325	-5.834	-5.790
Critical flow conditions, $r^*(Ca^*)$, eqn (24)			
$\log r_\infty^*$	0.067	-0.067	0.067
$\log r_0^*$	0.635	0.760	0.805
s_m	0.227	0.522	0.900
$\log Ca_m$	-5.325	-5.834	-5.790

781

782

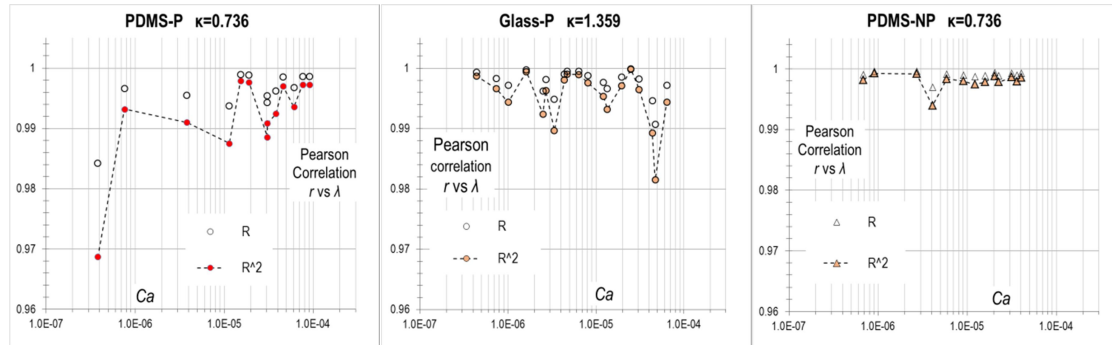
4.3 Paradigms of application in SCAL

783 The relative permeability scaling model, accounting for flow rate dependency, together with
784 the background theoretical framework (energy efficiency analysis, critical flow conditions
785 etc.) proposed by Valavanides [2023; 2018], have potential applications in SCAL and,
786 consequently, in reservoir engineering.

787 A central problem in SCAL is handling non-fully-developed flow conditions due to the
788 presence of capillary end effects. Fully developed flow is not a condition always attained in
789 SCAL measurements. The evolution of the interstitial flow, until fully developed flow
790 conditions are reached downstream the entry ports, depends on the structure of the pore
791 network, the wettability of the two-fluid/solid system and the superficial velocity of each
792 fluid. In general, end effects are pronounced when capillarity-associated phenomena are not
793 suppressed (overshadowed) by the prevailing viscous resistances. The analysis presented in
794 the current study can be applied in SCAL. Through the analysis of ex-core measurements
795 combined with a series of calculations—ranging from straightforward consistency checks
796 (e.g., comparison between imposed flow rate ratios and measured mobility ratios) to more
797 advanced assessments such as energy efficiency under varying flow conditions—it is possible
798 to identify the presence of end effects, quantify their magnitude, and characterize the pore
799 network (network typing).

800 As a paradigm in assessing the degree to which the co-injected flows in the different
801 networks have reached a fully-developed structure, we may focus on the diagrams in **Figure**
802 **8**. Note that the markers (\times) indicating values of the mobility ratio, λ_i , against, r_i , are – in
803 general – aligned along a straight line with gradient 1:1. In many cases, the two values are
804 practically equal, i.e. $\lambda_i = r_i$. For those cases, the kinetic states of the interstitial flow
805 structures, λ_i , are consistent to the externally imposed, kinematic constraints, r_i , indicating
806 that the corresponding flows are fully developed. Yet, in some diagrams pertaining to
807 constant- Ca_i , we may observe some degree of discrepancy between the mobility ratio and the
808 flow-rate ratio, manifested as a failure of the $\{\lambda_j, r_j\}_{Ca_i}$ markers to perfectly align to the

809 $r = \lambda$ straight line. That indicates these co-injections have not reached a fully-developed
 810 interstitial structure. We may evaluate the degree of misalignment and correlate it to the flow
 811 conditions and the two-fluid/network systems, by calculating the Pearson correlation
 812 coefficient between all sets of $\{\lambda_j, r_j\}_{Ca_i}$ pairs per Ca_i . The results for all the constant- Ca
 813 experiments in the three systems are presented in **Figure 12**.
 814



815

816 **Figure 12** Values of the Pearson correlation coefficient, R_i and R_i^2 , between flow-rate
 817 ratio r_i and mobility ratio, λ_i for the entire set of experiments conducted at various Ca_i in the
 818 three model pore networks.

819

820 We observe that the $\{\lambda_j, r_j\}_{Ca_i}$ misalignment from linearity is pronounced in the two
 821 periodic networks (PDMS-P & Glass-P) when compared with that of the non-periodic
 822 (PDMS-NP), indicating significant presence of end effects in the periodic networks. The
 823 source of the $\{\lambda_j, r_j\}_{Ca_i}$ misalignment may be attributed to the capillary end effects that are
 824 induced by the relatively stronger role of the menisci – when compared to the effects of the
 825 bulk viscosity. That may be attributed to the poorer interlacing of the two injected fluids
 826 upstream the network flow in the two periodic networks (PDM-P, Glass-P), compared to the
 827 single entry port of the PDMS-NP network – inciting a pre-mixing of the two fluids. We may
 828 also observe that the trends in the R_i^2 , values vs Ca , for the PDMS-P and the Glass-P systems
 829 are reversed. That is an interesting behavior, especially considering that the viscosity ratio
 830 values are inverse ($\kappa = 1/1.36 = 0.74$ in the PDMS-P and $\kappa = 1.36$ in the Glass-P system).
 831 Moreover, albeit the two networks have the same plane geometry they have different 3D
 832 structures, i.e. orthogonal pores with smooth surface (PDMS-P) against pores with slightly
 833 irregular shape and micro-roughness respectively (Glass-P).

834 In the same context, in many diagrams in **Figure 8**, pertaining to different constant- Ca
 835 experiments, the NWP and WP relative permeability curves intersect at the, so-called,
 836 relative permeability crossover flow-rate ratio value, $r_x = 1/\kappa$, eqn (11), indicated by the
 837 vertical dashed line. Yet, in some constant- Ca experiments the relative permeability
 838 crossover does not coincide with the theoretical value of r_x and that is something also
 839 observed for the low, R_i^2 , values, ref. **Figure 8** and **Figure 6**, indicating an underlying trend.

840 Energy efficiency analysis provides another paradigm on characterizing the flow system,
 841 in compliance to the normative methodology proposed in [Valavanides, 2018(b)]. Let us
 842 focus on the energy efficiency diagrams in **Figure 11** and, in particular, on the sigmoid
 843 curves interpolating the local maxima energy efficiency values $\{Ca_i, f_{EU,i}^*\}$. Based on these
 844 curves, for every two-fluid/network system, two nominal Ca values may be defined,
 845 corresponding to the apex of the two bends of the sigmoid curves. These bends segregate
 846 three distinct regions of the nominal Ca domain: the initial phase of the sigmoid curve,
 847 indicating low capillary flow conditions, the growth phase (sharp upward slope in the middle)
 848 indicating intermediate, capillary/viscous flow conditions, and the plateau phase (flattening-
 849 out) of the sigmoid curve indicating viscous flow conditions. This observation complies
 850 firmly with what we have observed (in section 3.3) with respect to the trends of the
 851 magnitude of the pressure fluctuations, as well as the time delay and the minimization of the
 852 associated fluctuations in the three pressure evolution diagrams in **Figure 5**.

853 These nominal values in Ca can be detected graphically or analytically, by setting the 2nd
 854 derivative of the expression (22), $d^2(\log f_{EU}^*)/dCa^2 = 0$ and solving for Ca . That of course
 855 comes at the extra cost of extensive measurements at various flow conditions to extract the
 856 maximum energy efficiency values and the CFCs. Yet, following the path of critical flow
 857 conditions will reduce the number of measurements. As discussed in [Valavanides *et al.*,
 858 2016] (ref. Fig. 3), if the co-injection conditions, (Ca, r) , are maintained along the CFCs,
 859 uncertainties associated with measurement errors is minimized and specificity is maximized –
 860 that is mainly attributed to the structure of the f_{EU} expression, eqs (12) or (19). Therefore,
 861 tracking and aligning to the CFCs path during the SCAL measurements can provide more
 862 accurate /unbiased information per unit cost of measurements.

863 Please note, no sophisticated technology is needed to implement the proposed
 864 methodology. The measurements of pressure and flow-rates are conventional measurements
 865 taken outside the core (ex-core measurements).

866 Moreover, the same, ex-core measurements are used to reveal the IDCP curve, which
 867 essentially provides the backbone of the flow-rate dependency description, eqn (13), of the
 868 two-fluid and core system. The form of the IDCP curve provides valuable information in
 869 assessing the extent of end effects and in deciphering the characteristics of the interstitial
 870 flow structure.

871 A convincing paradigm on how the IDCP curve may be used as a forensic tool in
 872 revealing the structure of the interstitial flow is provided in the systematic SCAL study
 873 performed by the IFP group on a core of natural Clashach sandstone [Valavanides *et al.*,
 874 2020]. An analysis of the measured relative permeabilities, similar to that described in
 875 paragraph 4.1, revealed a sharply decreasing intrinsic dynamic capillary pressure function,
 876 $A(\log Ca)$, over moderate- to /high- Ca flow conditions. That seemed to be contradicting the
 877 smooth, asymptotic transition to zero ($\log A \rightarrow 0$) depicted in **Figure 10** in the current study.
 878 Nevertheless the sharp decrease of A at moderate/high- Ca flow conditions was an indication
 879 of a sharp reduction of capillary resistances due to onset of emulsification.

880 In the current study, the trend in the IDCP functions, depicted in **Figure 10**, shows
881 asymptotic transitions to zero ($\log A \rightarrow 0$) at the high-end of Ca . This is consistent to video
882 observations of the interstitial flow structures comprising mixtures of connected WP and
883 intermittent flows of disconnected NWP fluidic elements. The latter are separated from the
884 WP through NWP/WP menisci remaining in contact to the pore walls. No signs of
885 emulsification were observed.

886 In addition, the generalized specific characteristic invariants, pertaining to the two-fluid
887 and pore network flow system, i.e. the locus of Critical Flow Conditions, the locus of cross-
888 over relative permeability conditions, as well as the Intrinsic Dynamic Capillary Pressure
889 curve, can be used as flow system identities and that could be a strong tool in developing
890 flow system characterization (“rock-typing”) methodologies and techniques.

891 In the reservoir engineering domain, the ability to handle a functional form of the relative
892 permeabilities, accounting for true-to-mechanism flow-rate dependency, through the IDCP
893 curve, can definitely improve the specificity of field-scale simulators. That can be achieved
894 by increasing the efficiency in physics-informed machine learning (PIML) interventions by
895 integrating the physical laws into machine learning models to improve prediction accuracy,
896 ensure physically plausible results, and reduce the need for massive data. The analysis based
897 on energy efficiency can be a powerful tool in assessing the operational efficiency of
898 enhanced oil recovery or CO₂ sequestration interventions, extending the energy transition
899 timelines of such energy intensive activities.

900 Future research, should focus on the deployment of a similar lab study in natural cores.

901

902 **Acknowledgements**

903 M. Valavanides acknowledges support from the German Academic Exchange Service
904 (DAAD-5752335 Research Stays for University Academics and Scientists, 2024) and from
905 the Univ. of West Attica for his sabbatical leave.

906 K. Mouravas acknowledges support from Erasmus+ KA131 Placement mobility.

907 H. Steeb and N. Karadimitriou would like to thank the Deutsche Forschungsgemeinschaft
908 (DFG, German Research Foundation) for supporting this work by funding SFB 1313, Project
909 Number 327154368.

910

911 **Data availability**

912 The datasets analyzed during the current study are available upon request to the
913 corresponding author.

914

915 **Contributions**

916 K. Mouravas - Methodology, Validation, Investigation, Data Curation, Visualization.

917 N. Karadimitriou - Methodology, Investigation, Resources, Data Curation, Project

918 administration.
919 P. Dimitriadis - Software, Formal analysis, Review.
920 A. Yiotis - Methodology, Review.
921 H. Steeb - Resources, Supervision, Project administration, Review.
922 M. Valavanides – Conceptualization, Methodology, Validation, Formal analysis, Data
923 Curation, Visualization, Supervision, Writing (Original Draft, Review & Editing).
924

925 **References**

- 926 API, American Petroleum Institute, 1998. Recommended Practice RP 40 “Recommended
927 Practices for Core Analysis” 2nd Edition, 1998.
- 928 Anastasiou, A., Zarikos, I., Yiotis, A., Talon, L., Salin, D., 2024. Steady-State Dynamics of
929 Ganglia Populations During Immiscible Two-Phase Flows in Porous Micromodels:
930 Effects of the Capillary Number and Flow Ratio on Effective Rheology and Size
931 Distributions, *Transport in Porous Media* **151**, 469-493, <https://doi.org/10.1007/s11242-023-02041-0>
932
- 933 Andrew M, Menke H, Blunt MJ, Bijeljic B., 2015. The imaging of dynamic multiphase fluid
934 flow using synchrotron-based X-ray microtomography at reservoir conditions. *Transp.*
935 *Porous Media* **110**, 1–24, <https://doi.org/10.1007/s11242-015-0553-2> .
- 936 Armstrong, R.T., McClure, J.E., Berrill, M.A., Rücker, M., Schlüter, S., Berg, S., 2016.
937 Beyond Darcy's law: The role of phase topology and ganglion dynamics for two-fluid
938 flow. *Phys. Rev. E* **94**, 043113, <https://doi.org/10.1103/PhysRevE.94.043113>
- 939 Aursjo, O., Erpelding, M., Tallakstad, K.T., Flekkøy, E.G., Hansen, A., Maloy, K.J., 2014.
940 Film flow dominated simultaneous flow of two viscous incompressible fluids through a
941 porous medium. *Frontiers in Physics* **2** (63), 1-9,
942 <https://doi.org/10.3389/fphy.2014.00063>
- 943 Avraam, D.G., Kolonis, G.B., Roumeliotis, T.C., Constantinides, G.N., Payatakes, A.C.,
944 1994. Steady-state two-phase flow through planar and nonplanar model porous media.
945 *Transp. Porous Media* **16**, 75–101, <https://doi.org/10.1007/BF01059777>
- 946 Avraam, D.G., Payatakes, A.C., 1995. Flow Regimes and Relative Permeabilities during
947 Steady-State Two-Phase Flow in Porous Media. *J. Fluid Mech.* **293**, 207-236,
948 <https://doi.org/10.1017/S0022112095001698>
- 949 Avraam, D.G., Payatakes, A.C., 1999. Flow Mechanisms, Relative Permeabilities and
950 Coupling Effects in Steady-State Two-Phase Flow in Porous Media. Case of Strong
951 Wettability. *Industrial & Engineering Chemistry Research* **38**(3), 778-786,
952 <https://doi.org/10.1021/ie980404o>
- 953 Bear, J., 2018, *Modeling Phenomena of Flow and Transport in Porous Media, Theory and*

- 954 *Applications of Transport in Porous Media*, Springer. ISBN: 978-3-319-72826-1 (eBook),
955 <https://doi.org/10.1007/978-3-319-72826-1>
- 956 Berg, S., Armstrong, R.T., Rücker, M., Hansen, A., Kjelstrup, S., Bedeaux, D., 2026. From
957 interface dynamics to Darcy scale description of multiphase flow in porous media.
958 *Advances in Colloid and Interface Science* **351** (103791), 1-65,
959 <https://doi.org/10.1016/j.cis.2026.103791>
- 960 Berg, S., Ott, H., Klapp, S. A., Schwing, A., Neiteler, R., Brussee, N., Makurat, A., Leu, L.,
961 Enzmann, F., Schwarz, J.-O., Wolf, F., Kersten, M., Irvine, S., Stampanoni, M., 2013.
962 Real-time 3D imaging of Haines jumps in porous media flow. *Proceedings of the National*
963 *Academy of Sciences*, **110**(10), 3755-3759, <https://doi.org/10.1073/pnas.1221373110>
- 964 Blunt, M.J., Jackson, M.D., Piri, M., Valvatne, P.H., 2002. Detailed physics, predictive
965 capabilities and macroscopic consequences for pore-network models of multiphase flow.
966 *Advances in Water Resources* **25** 1069-1089, [https://doi.org/10.1016/S0309-](https://doi.org/10.1016/S0309-1708(02)00049-0kjj)
967 [1708\(02\)00049-0kjj](https://doi.org/10.1016/S0309-1708(02)00049-0kjj)
- 968 Chevalier, T., Salin, D., Talon, L., Yiotis, A.G., 2015. History effects on nonwetting fluid
969 residuals during desaturation flow through disordered porous media. *Physical Review E*
970 **91**(4), 043015. <https://doi.org/10.1103/PhysRevE.91.043015>
- 971 Constantinides, G.N., Payatakes, A.C., 1989. A three dimensional Network Model for
972 Consolidated Porous Media. Basic Studies. *Chemical Engineering Communications* **81**,
973 55-81, <http://dx.doi.org/10.1080/00986448908940530>
- 974 Constantinides, G.N., Payatakes, A.C., 2000. Effects of Precursor Wetting Films in
975 Immiscible Displacement Through Porous Media. *Transport in Porous Media* **38**, 291–
976 317, <https://doi.org/10.1023/A:1006557114996>
- 977 Cueto-Felgueroso, L., Juanes, R., 2016. A discrete-domain description of multiphase flow in
978 porous media: Rugged energy landscapes and the origin of hysteresis. *Geophys. Res.*
979 *Lett.* **43**, 1615–1622, <https://doi.org/10.1002/2015GL067015>
- 980 Datta, S.S., Ramakrishnan, T.S., Weitz, D.A., 2014. Mobilization of a trapped non-wetting
981 fluid from a three dimensional porous medium, *Phys. Fluids* **26** (022002),
982 <https://doi.org/10.1063/1.4866641>
- 983 Datta, S.S., Dupin, J-B., Weitz, D.A., 2014. Fluid breakup during simultaneous two-phase
984 flow through a three-dimensional porous medium. *Physics of Fluids* **26**, 062004,
985 <https://doi.org/10.1063/1.4884955>
- 986 Dullien, F.A.L., 1992. *Porous media: fluid transport and pore structure* (2nd ed.). Academic
987 Press, San Diego, ISBN 978-0122236518.
- 988 Gao, Y., Lin, Q., Bijeljic, B., Blunt, M.J., 2020. Pore-scale dynamics and the multiphase
989 Darcy law. *Physical Review Fluids* **5**, 013801,
990 <https://doi.org/10.1103/PhysRevFluids.5.013801>

- 991 Georgiadis, A., Berg, S., Makurat, A., Maitland, G., Ott, H., 2013. Pore-scale
992 microcomputed-tomography imaging: Nonwetting-phase cluster-size distribution during
993 drainage and imbibitions. *Phys. Rev. E* **88**, 033002, 1-9,
994 <https://doi.org/10.1103/PhysRevE.88.033002>
- 995 Honarpour, M., Koederitz, L., Harvey, A.H., 1986. *Relative Permeability of Petroleum*
996 *Reservoirs*. Boca Raton, Florida, USA, CRC Press, ISBN 0-8493-5739-X
- 997 Karadimitriou, N.K., Joekar-Niasar, V., Hassanizadeh, S.M., Kleingeld, P. J., Pyrak-Nolte, L.
998 J., 2012. A novel deep reactive ion etched (DRIE) glass micro-model for two-phase flow
999 experiments. *Lab on a Chip* **12**, 3413–3418, <https://doi.org/10.1039/C2LC40530J>
- 1000 Karadimitriou, N. K., Musterd, M., Kleingeld, P. J., Kreutzer, M. T., Hassanizadeh, S. M.,
1001 Joekar-Niasar, V., 2013. On the fabrication of PDMS micromodels by rapid prototyping,
1002 and their use in two-phase flow studies. *Water Resources Research* **49** (4), 2056-2067,
1003 <https://doi.org/10.1002/wrcr.20196>
- 1004 Karadimitriou, N., Valavanides, M.S., Mouravas, K., Steeb, H., 2023. Flow Dependent
1005 Relative Permeability Scaling for Steady-State, Two-Phase Flow in Porous Media:
1006 Laboratory Validation on a Microfluidic Network. *Petrophysics* **64**(5), 656-679,
1007 <https://doi.org/10.30632/PJV64N5-2023a4>
- 1008 McPhee, C., Reed, J., Zubizarreta, I., 2015. *Core Analysis, A Best Practice Guide*. Elsevier,
1009 ISBN: 9780444636577
- 1010 Nguyen, V. H., Sheppard, A. P., Knackstedt, M. A., Pinczewski, W., 2006. The effect of
1011 displacement rate on imbibition relative permeability and residual saturation. *J. Petrol.*
1012 *Sci. Engng* **52**, 54–70, <http://dx.doi.org/10.1016/j.petrol.2006.03.020>
- 1013 Oughanem, R., Youssef, S., Bauer, D., Peysson, Y., Maire, E., Vizika, O., 2015. A Multi-
1014 Scale Investigation of Pore Structure Impact on the Mobilization of Trapped Oil by
1015 Surfactant Injection. *Transp. Porous Media* **109**, 673-692,
1016 <https://doi.org/10.1007/s11242-015-0542-5>
- 1017 Pak, T., Butler, I.B., Geiger, S., Dijke, M.I.J., Sorbie, K.S., 2015. Droplet fragmentation: 3D
1018 imaging of a previously unidentified pore-scale process during multiphase flow in porous
1019 media. *Proceedings of the National Academy of Sciences* **112**(7), 1947-1952,
1020 <https://doi.org/10.1073/pnas.1420202112>
- 1021 Reynolds, C.A., Menke, H., Andrew, M., Blunt, M.J., Krevor, S., 2017. Dynamic fluid
1022 connectivity during steady-state multiphase flow in a sandstone. *Proceedings of the*
1023 *National Academy of Sciences* **114** (31), 8187-81921-6,
1024 <https://doi.org/10.1073/pnas.1702834114>
- 1025 Rucker, M., Berg, S., Armstrong, R.T., Georgiadis, A., Ott, H., Schwing, A., Neiteler, R., N.
1026 Brussee, N., Makurat, A., Leu, L., Wolf, M., Khan, F., Enzmann, F., Kersten, M., 2015.
1027 From connected pathway flow to ganglion dynamics, *Geophys. Res. Lett.* **42**, 3888–3894,

- 1028 <https://doi.org/10.1002/2015GL064007>
- 1029 Rücker, M., Georgiadis, A., Armstrong, R.T., Ott, H., Brussee, N., van der Linde, H., Simon,
1030 L., Enzmann, F., Kersten, M., Berg, S., 2021. The Origin of Non-thermal Fluctuations in
1031 Multiphase Flow in Porous Media. *Front. Water* **3**, 671399, 1–25,
1032 <https://doi.org/10.3389/frwa.2021.671399>
- 1033 Singh, K., Bijeljic, B., Blunt, M.J., 2016. Imaging of oil layers, curvature and contact angle in
1034 a mixed-wet and a water-wet carbonate rock. *Water Resour. Res.* **52**, 1716–1728,
1035 <https://doi.org/10.1002/2015WR018072>
- 1036 Sinha, S. Bender, A.T., Danczyk, M., Keepseagle, K., Prather, C.A., Bray, J.M., Thrane,
1037 L.W., Seymour, J.D., Codd, S.I., Hansen, A., 2017. Effective Rheology of Two-Phase
1038 Flow in Three-Dimensional Porous Media: Experiment and Simulation. *Transport in*
1039 *Porous Media* **119**(1), 77-94, <http://dx.doi.org/10.1007/s11242-017-0874-4>
- 1040 Sinha, S., Gjennestad, M.A., Vassvik, M., Hansen, A., 2021. Fluid Meniscus Algorithms for
1041 Dynamic Pore-Network Modeling of Immiscible Two-Phase Flow in Porous Media.
1042 *Front. Phys.* **8**:548497, <https://doi.org/10.3389/fphy.2020.548497>
- 1043 Spurin, C., Bultreys, T., Bijeljic, B., Blunt, M.J., 2019. Intermittent fluid connectivity during
1044 two-phase flow in a heterogeneous carbonate rock. *Physical Review E* **100**, 043103, 1-
1045 10, <https://doi.org/10.1103/PhysRevE.100.043103>
- 1046 Tallakstad, K.T., Knudsen, H.A., Ramstad, T., Løvoll, G., Maløy, K.J., Toussaint, R.,
1047 Flekkøy, E.G., 2009. Steady-State Two-Phase Flow in Porous Media: Statistics and
1048 Transport Properties. *Physical Review Letters* **102** 074502, 1-4,
1049 <https://doi.org/10.1103/PhysRevLett.102.074502>
- 1050 Tsakiroglou, C.D., Aggelopoulos, C.A., Terzi, K., Avraam, D.G., Valavanides, M.S., 2015.
1051 Steady-state two-phase relative permeability functions of porous media: A revisit.
1052 *International Journal of Multiphase Flow* **73**, 34–42,
1053 <http://dx.doi.org/10.1016/j.ijmultiphaseflow.2015.03.001>
- 1054 Valavanides, M.S., Constantinides, G.C., Payatakes, A.C., 1998. Mechanistic Model of
1055 Steady-State Two-Phase Flow in Porous Media Based on Ganglion Dynamics. *Transport*
1056 *in Porous Media* **30**, 267–299, <https://doi.org/10.1023/A:1006558121674>
- 1057 Valavanides, M.S., Daras, T., 2016. Definition and Counting of Configurational Microstates
1058 in Steady-State Two-Phase Flows in Pore Networks. *Entropy* **18** (054), 1-28,
1059 <http://doi:10.3390/e18020054>
- 1060 Valavanides, M.S., Payatakes, A.C., 2001. True-to-Mechanism Model of Steady-State Two-
1061 Phase Flow in Porous Media, using Decomposition into Prototype Flows. *Advances in*
1062 *Water Resources* **24** (3-4), 385-407, [https://doi.org/10.1016/S0309-1708\(00\)00063-4](https://doi.org/10.1016/S0309-1708(00)00063-4)

- 1063 Valavanides, M.S., Totaj, E., Tsokopoulos, M., 2016. Energy Efficiency Characteristics in
1064 Steady-State Relative Permeability Diagrams of Two-Phase Flow in Porous Media. *J.*
1065 *Pet. Sci. Eng.* **147**, 181-201 <http://dx.doi.org/10.1016/j.petrol.2016.04.039>
- 1066 Valavanides, M.S., Daras, T., 2016. Definition and Counting of Configurational Microstates
1067 in Steady-State Two-Phase Flows in Pore Networks. *Entropy* **18** (054), 1-28,
1068 <http://dx.doi.org/10.3390/e18020054>
- 1069 Valavanides, M.S., 2018(a). Oil fragmentation, interfacial surface transport and flow
1070 structure maps for two-phase flow in model pore networks. Predictions based on
1071 extensive, DeProF model simulations. *Oil & Gas Science and Technology - Rev. IFP*
1072 *Energies nouvelles* **73** (6), 1-36, <https://doi.org/10.2516/ogst/2017033>
- 1073 Valavanides, M.S., 2018(b). Review of steady-state two-phase flow in porous media:
1074 independent variables, universal energy efficiency map, critical flow conditions,
1075 effective characterization of flow and pore network *Transp. in Porous Media* **123** (1),
1076 42-99, <https://doi.org/10.1007/S11242-018-1026-1>
- 1077 Valavanides, M.S., Masclé, M., Youssef, S., Vizika, O., 2020. Steady-State Two-Phase Flow
1078 in Porous Media: Laboratory Validation of Flow Dependent Relative Permeability
1079 Scaling. *E3S Web of Conferences* **146**, 03002, The International Symposium of the
1080 Society of Core Analysts, SCA2019, <https://doi.org/10.1051/e3sconf/202014603002>
- 1081 Valavanides, M.S., 2023. Flow-rate Dependency of Steady-State Two-Phase Flows in Pore
1082 Networks: Universal, Relative Permeability Scaling Function and System Characteristic
1083 Invariants. *Transp. in Porous Media* **150**, 521-557. [https://doi.org/10.1007/s11242-023-](https://doi.org/10.1007/s11242-023-02012-5)
1084 [02012-5](https://doi.org/10.1007/s11242-023-02012-5)
- 1085 Wang, X., Li, S., Lv, P., Liang, C., Xu, J., Shi, M., Tong, B., Jiang, L., Liu, Y., Song, Y.,
1086 2025. Pore-scale intermittent flow and its impact on two-phase fluid distribution in
1087 porous media. *Water Resources Research* **61**, e2025WR040858.
1088 <https://doi.org/10.1029/2025WR040858>
- 1089 Wildenschild, D., Hopmans, J.W., Simunek, J., 2001. Flow rate dependence of soil hydraulic
1090 characteristics. *Soil Sci. Soc. Am. J.* **65**, 35–48, <https://doi.org/10.2136/sssaj2001.65135x>
- 1091 Wildenschild D, Sheppard A.P., 2013. X-ray imaging and analysis techniques for quantifying
1092 pore-scale structure and processes in subsurface porous medium systems. *Advances in*
1093 *Water Resources* **51**, 217–246, <http://dx.doi.org/10.1016/j.advwatres.2012.07.018>
- 1094 Wegner, M.W., Christie, J.M., 1983. Chemical etching of deformation sub-structures in
1095 quartz. *Phys Chem Minerals* **9**, 67–78, <https://doi.org/10.1007/BF00308150>
- 1096 Wyckoff, R.D., Botset, H.G., 1936. The Flow of Gas-Liquid Mixtures Through
1097 Unconsolidated Sands. *Physics* **7**, 325-345, <https://doi.org/10.1063/1.1745402>
- 1098 Xia, Y., Whitesides, G.M., 1998. Soft Lithography. *Annual Review of Materials Science* **28**,
1099 153-184, <https://doi.org/10.1146/annurev.matsci.28.1.153>

- 1100 Yang, M., Liu, C., Li, Z., Li, Y., Du, D., 2026. Numerical evaluation of the pore structure
1101 effect-incorporated capillary number on the characterization of the immiscible two-phase
1102 displacement process in porous media. *Chemical Engineering Science*, PII: S0009-
1103 2509(26)00727-X, <https://doi.org/10.1016/j.ces.2026.124015>
- 1104 Yiotis, A.G., Dollari, A., Kainourgiakis, M.E., 2019. Nonlinear Darcy flow dynamics during
1105 ganglia stranding and mobilization in heterogeneous porous domains. *Physical Review*
1106 *Fluids* **4** 114302, <https://doi.org/10.1103/PhysRevFluids.4.114302>
- 1107 Youssef, S., Rosenberg, E., Deschamps, H., Oughanem, R., Maire, E., Mokso, R., 2014. Oil
1108 ganglia dynamics in natural porous media during surfactant flooding captured by ultra-
1109 fast x-ray microtomography. SCA 2014-23, *Intern. Symposium of the Society of Core*
1110 *Analysts*, France, 11-18 Sept, 1-12
- 1111 Youssef, S., Mascle, M., Peysson, P., Vizika, O., 2017. CAL X: An X Ray Radiography Tool
1112 for High Throughput Coreflood Experimentation. Applications in the EOR Context.
1113 SCA2017-12, *Int. Symp. Soc. Core Analysts*, Vienna, Austria 28 Aug. - 1 Sept., 1-12
- 1114 Zhang, Y., Bijeljic, B., Gao, Y., Lin, Q., Blunt, M. J., 2021. Quantification of nonlinear
1115 multiphase flow in porous media. *Geophysical Research Letters* **48**, e2020GL090477.
1116 <https://doi.org/10.1029/2020GL090477>
- 1117 Zou, S., Armstrong, R. T., Arns, J.-Y., Arns, C. H., Hussain, F., 2018. Experimental and
1118 theoretical evidence for increased ganglion dynamics during fractional flow in mixed-
1119 wet porous media. *Water Resources Research* **54**, 3277-3289.
1120 <https://doi.org/10.1029/2017WR022433>
- 1121

Declaration of interests

The authors declare that they have no known competing financial interests or personal relationships that could have appeared to influence the work reported in this paper.

The authors declare the following financial interests/personal relationships which may be considered as potential competing interests: